

---

# ON RETROSPECTIVE $k$ -SPACE SUBSAMPLING SCHEMES FOR DEEP MRI RECONSTRUCTION

---

**George Yiasemis**  
Netherlands Cancer Institute,  
Amsterdam, 1066 CX,  
the Netherlands  
g.yiasemis@nki.nl

**Clara I. Sánchez**  
qurAI group  
University of Amsterdam,  
Amsterdam, 1012 WX,  
the Netherlands  
c.i.sanchezgutierrez@uva.nl

**Jan-Jakob Sonke**  
Netherlands Cancer Institute,  
Amsterdam, 1066 CX,  
the Netherlands  
j.sonke@nki.nl

**Jonas Teuwen**  
Netherlands Cancer Institute,  
Amsterdam, 1066 CX,  
the Netherlands  
j.teuwen@nki.nl

January 25, 2023

## ABSTRACT

**Purpose:** The MRI  $k$ -space acquisition is time consuming. Traditional techniques aim to acquire accelerated data, which in conjunction with recent DL methods, aid in producing high-fidelity images in truncated times. Conventionally, subsampling the  $k$ -space is performed by utilizing Cartesian-rectilinear trajectories, which even with the use of DL, provide imprecise reconstructions, though, a plethora of non-rectilinear or non-Cartesian trajectories can be implemented in modern MRI scanners. This work investigates the effect of the  $k$ -space subsampling scheme on the quality of reconstructed accelerated MRI measurements produced by trained DL models.

**Methods:** The RecurrentVarNet was used as the DL-based MRI-reconstruction architecture. Cartesian fully-sampled multi-coil  $k$ -space measurements from three datasets with different accelerations were retrospectively subsampled using eight distinct subsampling schemes (four Cartesian-rectilinear, two Cartesian non-rectilinear, two non-Cartesian). Experiments were conducted in two frameworks: Scheme-specific, where a distinct model was trained and evaluated for each dataset-subsampling scheme pair, and multi-scheme, where for each dataset a single model was trained on data randomly subsampled by any of the eight schemes and evaluated on data subsampled by all schemes.

**Results:** In the scheme-specific setting RecurrentVarNets trained and evaluated on non-rectilinearly subsampled data demonstrated superior performance especially for high accelerations, whilst in the multi-scheme setting, reconstruction performance on rectilinearly subsampled data improved when compared to the scheme-specific experiments.

**Conclusion:** Training DL-based MRI reconstruction algorithms on non-rectilinearly subsampled measurements can produce more faithful reconstructions. Our findings demonstrate the potential for using DL-based methods trained on prospective acquisitions with non-rectilinearly subsampled measurements to optimize scan time and image quality.

**Keywords** Deep MRI Reconstruction, Retrospective  $k$ -space Subsampling, Non-rectilinear Subsampling, Non-Cartesian Subsampling, Recurrent Variational Network

# 1 Introduction

Magnetic Resonance Imaging (MRI) is one of the most important imaging modalities in medicine. MRI's non-invasive nature, non-use of ionizing radiation, and ability to produce high-resolution images make it a valuable technique for a wide range of clinical applications, including diagnosis, treatment planning, and dynamic tasks such as MR-guided surgery or radiotherapy. However, the application of MRI to dynamic tasks has been limited by the long acquisition times required. MRI measurements, known as the  $k$ -space, are acquired sequentially, resulting in prolonged scanning times.

Over the past two decades, several methods have been put to use in clinical practice for accelerating the MRI acquisition. The two most conventionally applied methods to-date are Parallel Imaging (PI) and Compressed Sensing (CS), which are usually both incorporated in modern state-of-the-art MRI scanners.

Compressed Sensing aims in reconstructing images from subsampled  $k$ -space measurements [1, 2, 3, 4]. Subsampling the  $k$ -space is, in general, a violation of the Nyquist-Shannon sampling criterion [5] and reconstructions of subsampled data are prone to producing aliasing artifacts. CS reconstruction algorithms attempt to solve minimization problems such as Total Variation (TV) optimization [6] that given a sparse low-dimensional input signals, aim to reconstruct high-dimensional images.

Parallel Imaging on the other hand, employs an array of multiple - instead of one - radio-frequency receiver coils which measure reduced sets of spatially localised  $k$ -space frequencies while maintaining the same spatial resolution [7, 8, 9]. Each independent receiver coil receives distinct measurements corresponding to their spatial location in relation to the scanned object. Hence, for each coil a unique sensitivity profile-map exists, that encodes its spatial sensitivity. Sensitivity maps are either known or estimated by performing a pre-scan. In Figure 1 we provide an example of a PI acquisition from a MRI scanner with  $n_c = 16$  coils.

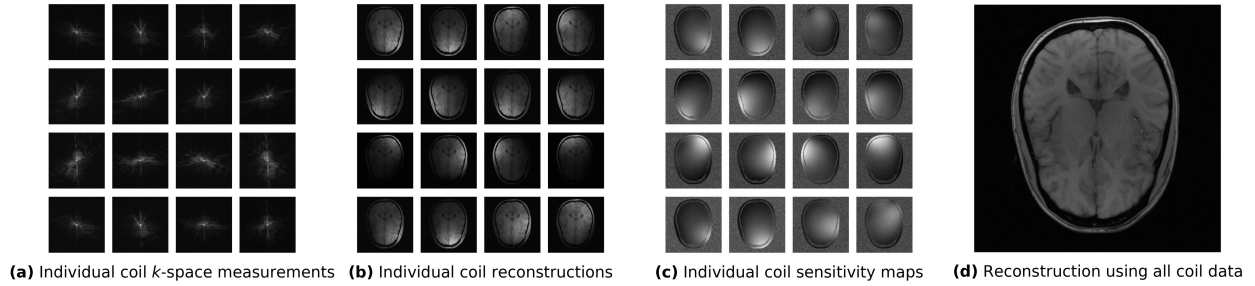


Figure 1: Parallel Imaging: Acquisition of  $k$ -space measurements from a 16-coil array machine. The reconstructed image can be obtained by combining the individual coil reconstructions using the root-sum-of-squares (RSS) method.

With the recent advancements in Deep Learning (DL) and Computer Vision (CV), a plethora of algorithms have emerged targeting to solve imaging inverse problems, with Accelerated MRI Reconstruction being a par excellence example. Combined with CS and PI, numerous DL-based methods involving convolutional neural networks (CNNs) have been proposed in the literature [10, 11, 12, 13, 14, 15, 16, 17] applied to the task of Accelerated MRI Reconstruction. These methods are usually trained in a supervised manner using retrospectively subsampled (from available fully-sampled)  $k$ -space datasets and their target is to make a prediction of the fully-sampled  $k$ -space or its image reconstruction.

Rectilinear Cartesian patterns constitute the most commonly employed (prospective) sampling and subsampling techniques applied in clinical settings. Subsequently, DL-based Accelerated MRI Reconstruction applications utilize rectilinear subsampling masks to retrospectively subsample fully-sampled data. However, a variety of prospective and retrospective sampling and subsampling patterns exist with the majority of them not being rectilinear Cartesian. For instance, non-Cartesian patterns such as radial or spiral have been shown to be applied in real-time MRI acquisitions due to the fact that they are less susceptible to motion compared to Cartesian ones [18]. The authors in [19] by employing a deep neural network architecture, namely the Recurrent Inference Machine (RIM) [13], explored the effects of training RIMs by applying either rectilinear or radial retrospective subsampling and concluded that the RIM trained using the latter can produce higher-fidelity reconstructions.

In this work, we aim to investigate and compare the effects of employing miscellaneous retrospective subsampling schemes on the quality of DL-based learned image reconstructions. To that end, we trained and tested Recurrent Variational Networks [10] (RecurrentVarNets) on retrospectively subsampled  $k$ -space measurements. We performed experiments under either scheme-specific or multi-scheme setups, in which models were trained and evaluated on data subsampled with either individual and multiple, respectively, subsampling schemes.



The contributions and findings of our work can be summarized as follows:

- We provide a review of eight currently employed (retrospective) subsampling techniques.
- We experimentally show that DL models trained and evaluated on non-rectilinearly, compared to rectilinearly, subsampled data output superior reconstructions, especially for high acceleration factors.
- We demonstrate that models trained on data subsampled with multiple instead of individual patterns, can reconstruct rectilinearly subsampled data with higher fidelity.

## 2 Background - Theory

### 2.1 MRI Acquisition

MRI reconstruction is an inverse problem on account of the fact that MR scanners acquire MRI measurements in the frequency domain, also known as the Fourier space, and an inversion procedure is required to produce the desired MR image.

Let  $n = n_x \times n_y$  denote the spatial size of the reconstructed data. In the case of single-coil acquisition, the relationship between the underlying (vectorized) image  $\mathbf{x} \in \mathbb{C}^n$  and the (vectorized) single-channel  $k$ -space  $\mathbf{y} \in \mathbb{C}^n$  is given by

$$\mathbf{y} = \mathcal{F}(\mathbf{x}) + \mathbf{e}, \quad (1)$$

where  $\mathcal{F}$  denotes the two-dimensional (Fast) Fourier Transform (FFT) and  $\mathbf{e} \in \mathbb{C}^n$  some measurement noise.

#### 2.1.1 Parallel MRI Acquisition

In PI multiple receiver coils are placed around the subject to speed up the acquisition. Assuming a number of  $n_c$  coils, the acquired (multi-channel)  $k$ -space measurements are given by

$$\begin{aligned} \mathbf{y} &= (\mathbf{y}^1, \dots, \mathbf{y}^{n_c}) \in \mathbb{C}^{n \times n_c}, \\ \mathbf{y}^k &= \mathcal{F}(\mathbf{S}^k \mathbf{x}) + \mathbf{e}^k, \quad k = 1, 2, \dots, n_c, \end{aligned} \quad (2)$$

where  $\mathbf{e}^k$  denotes noise measured by the  $k^{\text{th}}$  coil and  $\mathbf{S}^k \in \mathbb{C}^{n \times n}$  the sensitivity map of the  $k^{\text{th}}$  coil expressed as a diagonal complex matrix. Within each coil's reception region, these maps encode their spatial sensitivity by measuring the relative weighting of signals acquired from various locations around the subject. The sensitivity maps are usually normalized as follows

$$\sum_{k=1}^{n_c} \mathbf{S}^{k*} \mathbf{S}^k = \mathbf{I}_n, \quad (3)$$

where  $\mathbf{S}^{k*}$  indicates the complex conjugate of  $\mathbf{S}^k$  and  $\mathbf{I}_n \in \mathbb{R}^{n \times n}$  denotes the  $n$ -rank identity matrix.

Obtaining an image from multi-channel measurements  $\mathbf{y}$  can be done by either using the root-sum-of-squares (RSS) or the SENSE methods which operate as follows:

$$\mathbf{x}_{\text{rss}} = \text{RSS}(\hat{\mathbf{x}}^1, \dots, \hat{\mathbf{x}}^{n_c}) = \left( \sum_{k=1}^{n_c} |\hat{\mathbf{x}}^k|^2 \right)^{\frac{1}{2}} \quad (4)$$

and,

$$\begin{aligned} \mathbf{x}_{\text{sense}} &= |\text{SENSE}(\hat{\mathbf{x}}^1, \dots, \hat{\mathbf{x}}^{n_c})| = \left| \sum_{k=1}^{n_c} \mathbf{S}^{k*} \hat{\mathbf{x}}^k \right|, \\ \hat{\mathbf{x}}^k &= \mathcal{F}^{-1}(\mathbf{y}^k), \quad k = 1, 2, \dots, n_c. \end{aligned} \quad (5)$$

### 2.2 Accelerated MRI Acquisition

To accelerate the MRI acquisition, in CS settings the  $k$ -space is subsampled by collecting fewer than necessary measurements. The subsampling procedure can be described as the application of a subsampling operator  $\mathbf{U}$  on the fully-sampled  $k$ -space measurements. The subsampled  $k$ -space is given by

$$\tilde{\mathbf{y}}^k = \mathbf{U} \mathbf{y}^k = \mathbf{U} \mathcal{F}(\mathbf{S}^k \mathbf{x}) + \tilde{\mathbf{e}}^k, \quad k = 1, 2, \dots, n_c, \quad (6)$$

where  $\mathbf{U} \in \{0, 1\}^n$  is expressed as a binary diagonal mask, and indicates which measurements are sampled as follows:

$$\mathbf{z}_{\mathbf{U}} := (\mathbf{U}\mathbf{z})_i = \begin{cases} \mathbf{z}_i, & \mathbf{U}_{ii} = 1 \\ 0, & \mathbf{U}_{ii} = 0. \end{cases} \quad (7)$$

The magnitude of the acceleration is determined by an acceleration factor  $R$ . For a specific  $R$ ,  $\mathbf{U}$  can be chosen such that

$$n \cdot \left( \sum_{i=1}^n \mathbf{U}_{ii} \right)^{-1} \approx R. \quad (8)$$

## 2.3 Accelerated MRI Reconstruction

### 2.3.1 Sensitivity Map Estimation

The sensitivity maps  $\mathbf{S} = (\mathbf{S}^1, \dots, \mathbf{S}^{n_c})$  can be estimated by various methods found in the literature [20, 8, 21, 22]. A common method for estimating them is by fully-sampling a small region of the center of the  $k$ -space, also known as the autocalibration signal (ACS) which includes low frequencies [11, 10].

Let  $\mathbf{U}_{\text{ACS}} \in \{0, 1\}^n$  denote the ACS-subsampling operator such that when applied on  $k$ -space data it outputs the fully-sampled ACS region, i.e.:

$$\mathbf{z}_{\text{acs}} := (\mathbf{U}_{\text{ACS}}\mathbf{z})_i = \begin{cases} \mathbf{z}_i, & i \in \text{ACS region} \\ 0, & \text{otherwise.} \end{cases} \quad (9)$$

Subsequently, to obtain an initial approximation of the sensitivity maps we use the root-sum-of-squares (RSS) method:

$$\tilde{\mathbf{S}}^k \approx \text{diag} \left[ \mathbf{x}_{\text{acs}}^k \oslash \mathbf{x}_{\text{acs}} \right], \quad k = 1, 2, \dots, n_c, \quad (10)$$

where  $\oslash$  denotes the element-wise division, and

$$\mathbf{x}_{\text{acs}}^k = \mathcal{F}^{-1}(\mathbf{U}_{\text{ACS}}\tilde{\mathbf{y}}^k), \quad \mathbf{x}_{\text{acs}} = \text{RSS} \left( \left\{ \mathbf{x}_{\text{acs}}^k \right\}_{k=1}^{n_c} \right). \quad (11)$$

### 2.3.2 Accelerated MRI Reconstruction as an Inverse Problem

Obtaining a reconstruction from accelerated multicoil  $k$ -space measurements is an inverse problem, with a forward problem given by Eq. 6. We can rewrite Eq. 6 in a more compact notation:

$$\tilde{\mathbf{y}} = \mathcal{A}_{\mathbf{U},\mathbf{S}}(\mathbf{x}), \quad \mathcal{A}_{\mathbf{U},\mathbf{S}} := \mathbf{U} \circ \mathcal{F} \circ \mathcal{E}_{\mathbf{S}} \quad (12)$$

where  $\mathcal{A}_{\mathbf{U},\mathbf{S}} : \mathbb{C}^n \rightarrow \mathbb{C}^{n \times n_c}$  denotes the forward operator and  $\mathcal{E}_{\mathbf{S}} : \mathbb{C}^n \rightarrow \mathbb{C}^{n \times n_c}$  is called the expand operator which maps an image  $\mathbf{w} \in \mathbb{C}^n$  to the individual coil images using  $\mathbf{S}$ :

$$\mathcal{E}_{\mathbf{S}}(\mathbf{w}) = (\mathbf{S}^1\mathbf{w}, \dots, \mathbf{S}^{n_c}\mathbf{w}). \quad (13)$$

The backward operator of  $\mathcal{A}_{\mathbf{U},\mathbf{S}}$  is given by

$$\mathcal{A}_{\mathbf{U},\mathbf{S}}^* := \mathcal{R}_{\mathbf{S}} \circ \mathcal{F}^{-1} \circ \mathbf{U} : \mathbb{C}^{n \times n_c} \rightarrow \mathbb{C}^n, \quad (14)$$

where  $\mathcal{R}_{\mathbf{S}} : \mathbb{C}^{n \times n_c} \rightarrow \mathbb{C}^n$  is called the reduce operator that combines individual coil images  $\mathbf{z} \in \mathbb{C}^{n \times n_c}$  using  $\mathbf{S}$  as follows:

$$\mathcal{R}_{\mathbf{S}}(\mathbf{z}) = \sum_{k=1}^{n_c} \mathbf{S}^{k*} \mathbf{z}^k. \quad (15)$$

Note that the operators  $\mathbf{U}$ ,  $\mathcal{F}$  and  $\mathcal{F}^{-1}$  in Eq. 12 and Eq. 14 are applied coil-wise.

Subsampling the  $k$ -space causes obtaining a solution to Eq. 12 to be an ill-posed inverse problem [23, 24], and therefore, a solution through direct inversion is not feasible. Conventionally, in CS recovering an estimation of the ground truth image  $\mathbf{x}$  from the subsampled MRI measurements  $\tilde{\mathbf{y}}$  can be formulated as a solution to a variational optimization problem as follows:

$$\hat{\mathbf{x}} = \underset{\mathbf{w}}{\text{argmin}} \left\| \mathcal{A}_{\mathbf{U},\mathbf{S}}(\mathbf{w}) - \tilde{\mathbf{y}} \right\|_2^2 + \alpha \mathcal{G}(\mathbf{w}), \quad (16)$$

where  $\mathcal{G} : \mathbb{C}^n \rightarrow \mathbb{R}$  is a regularization function which can impose prior information about the solution and  $\alpha > 0$  is a regularization parameter. In the literature various choices of  $\mathcal{G}$  and algorithms for solving Eq. 16 have been employed [25, 26, 27, 28].

### 2.3.3 Deep Learning-based Accelerated MRI Reconstruction

With the advent of the involvement of DL in MRI reconstruction tasks, the need for handcrafting a specific regularization function has been replaced with CNN-based architectures. A plethora of approaches solve Eq. 16 by unrolling it into a gradient descent iterative optimization scheme over  $T$  time-steps:

$$\begin{aligned} \mathbf{w}_{t+1} &= \mathbf{w}_t - \alpha_{t+1} \mathcal{A}_{\mathbf{U}, \mathbf{S}}^* (\mathcal{A}_{\mathbf{U}, \mathbf{S}}(\mathbf{w}_t) - \tilde{\mathbf{y}}) + \mathcal{H}_{\theta_{t+1}}(\mathbf{w}_t), \\ t &= 0, \dots, T-1, \end{aligned} \quad (17)$$

where  $\alpha_t$  denotes a (trainable) learning rate and  $\mathcal{H}_{\theta_t}$  a CNN-based architecture with trainable parameters  $\theta_t$ . The initial image  $\mathbf{w}_0$  in Eq. 17 can be chosen as a zero-filled reconstruction using  $\tilde{\mathbf{y}}$  as in Eq. 4 or Eq. 5.

Sensitivity maps can be estimated as in Eq. 10 and/or can be refined using another CNN-based model  $\mathcal{S}_\psi$  with trainable parameters  $\psi$  which takes as input the estimation  $\tilde{\mathbf{S}} = (\tilde{\mathbf{S}}^1, \dots, \tilde{\mathbf{S}}^{n_e})$  as in Eq. 10:

$$\mathbf{S} = \mathcal{S}_\psi(\tilde{\mathbf{S}}). \quad (18)$$

Optimization of Eq. 17 may alternatively be performed in the  $k$ -space domain as demonstrated by some authors [10, 11]:

$$\begin{aligned} \mathbf{y}_{t+1} &= \mathbf{y}_t - \alpha_{t+1} \mathbf{U}(\mathbf{y}_t - \tilde{\mathbf{y}}) + \\ &\quad \mathcal{F} \circ \mathcal{E}_\mathbf{S} \circ \mathcal{H}_{\theta_{t+1}} \circ \mathcal{R}_\mathbf{S} \circ \mathcal{F}^{-1}(\mathbf{y}_t), \quad \mathbf{y}_0 = \tilde{\mathbf{y}}. \end{aligned} \quad (19)$$

The architecture we opted for is based on Eq. 19.

### 2.4 $k$ -space Sampling

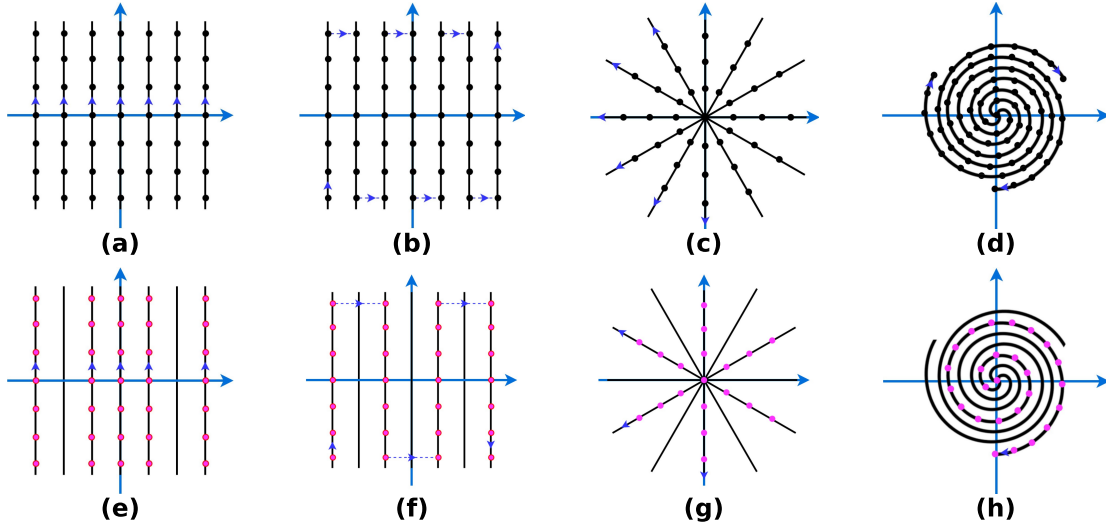


Figure 2: **Top:**  $k$ -space sampling trajectories. Cartesian: (a) Rectilinear:  $k$ -space is filled in a line-by-line scheme, (b) EPI:  $k$ -space is filled in a rectilinear way but in one shot ("zig-zag"). Non-Cartesian (c) Radial:  $k$ -space is filled with radial spokes passing through the center, (d) Spiral:  $k$ -space is filled by one or multiple helical curves. Each line in (a), (b) and (c) and each curve in (d) represents a separate filling. The dark blue arrows show the direction of each readout. **Bottom:** Subsampled  $k$ -space trajectories for different acceleration factors: (e) Rectilinear,  $R \approx 1.5$ . (f) EPI,  $R \approx 1.75$ . (g) Radial,  $R \approx 2$ . (h) Spiral,  $R \approx 3$ .

A sampling scheme or  $k$ -space trajectory refers to the course of filling up a complex array with  $k$ -space frequencies acquired over a sequence of time-steps during the MRI acquisition. There exist a wide range of  $k$ -space trajectories implemented in clinical settings which can be split into two groups: Cartesian and non-Cartesian trajectories. Figure 2(a)-(d) depicts two of each.

Cartesian trajectories aim in collecting samples on a Cartesian or equispaced and rectangular grid. The most common Cartesian trajectory is the rectilinear one in which  $k$ -space samples are acquired in a line-by-line scheme as illustrated by Figure 2(a) with resulting samples being equidistant in both axes. Note that usually in the literature the Cartesian

rectilinear trajectory is referred to as simply *Cartesian*. In this work we use the characterization *Cartesian* to refer to any trajectory acquired on a Cartesian grid. Other Cartesian trajectories include the Echo-planar imaging (EPI) in which  $k$ -space lines are acquired in a rectilinear fashion but in a "zig-zag" pattern as shown by Figure 2(b).

Non-Cartesian trajectories include schemes such as the radial or the spiral. In the former the  $k$ -space signal samples are acquired along several spokes crossing its center (see Figure 2(c)) with a result the center being sampled multiple times, while the latter includes acquiring data on single or multiple helical curves starting from the center of the  $k$ -space (see Figure 2(d)). In non-Cartesian trajectories  $k$ -space measurements are acquired on a non-Cartesian grid and are therefore not equidistant with each other. For instance, in the radial filling samples closer to the center are more dense compared to samples further on the radial spokes.

To accelerate the MRI acquisition, the  $k$ -space is subsampled by an acceleration factor  $R$ , resulting in fewer measurements being collected than those strictly required by the Nyquist-Shannon criterion for perfect reconstruction. This can lead to a degradation of the quality of the reconstruction, depending on the magnitude of the acceleration factor. For instance, for  $R = 2$ , half of the necessary  $k$ -space measurements are acquired. In Figure 2(e)-(h) we provide examples of subsampled  $k$ -space trajectories: Cartesian rectilinear and EPI (Figures 2(e)-(f)), radial and spiral (Figure 2(g)-(h)).

### 3 Methods

#### 3.1 Retrospective $k$ -space Subsampling

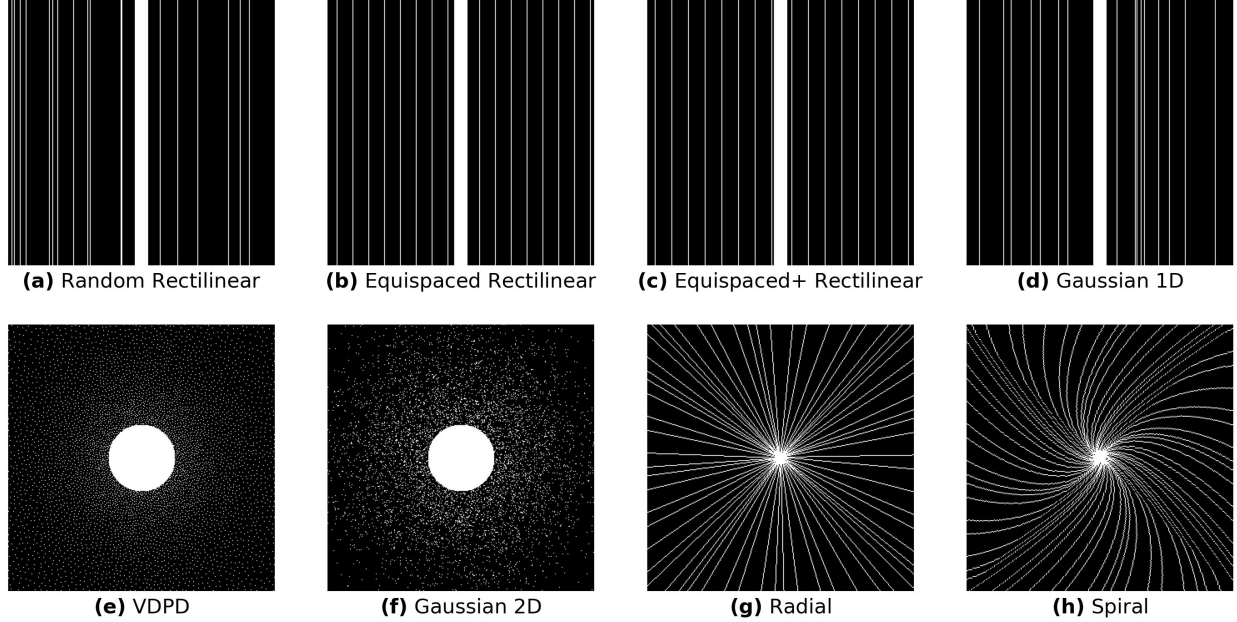


Figure 3: Examples of subsampling masks for Cartesian data for acceleration factor  $R = 5$ . **(a)-(d)** Rectilinear: generated by first selecting a fraction of ACS columns and then the rest of the columns (a) are selected uniformly at random, (b) are equispaced with a fixed distance, (c) are equispaced but symmetric, (d) are selected from the Gaussian distribution **(e)** Variable-density Poisson Disk: generated by fully-sampling a centered disk for the ACS region and then applying the Bridson’s fast algorithm [29]. **(f)** Gaussian 2D: samples selected from a 2D Gaussian distribution. **(g)-(h)** Simulated non-Cartesian using the CIRCUS algorithm [30]: (g) Radial, (h) Spiral.

The data used in this work consisted of volumes of fully-sampled raw  $k$ -space measurements acquired on a Cartesian grid. To simulate prospective subsampling we generated subsampling masks which we retrospectively applied onto the fully-sampled multi-coil  $k$ -space data to produce subsampled/masked measurements. The generated subsampling masks were binary signifying that a sample from the fully-sampled data was masked if and only if the corresponding mask entry was zero.

As in this work we are interested in studying the role of the subsampling pattern on the quality of DL-based reconstructions of subsampled MRI data, we focused on the following retrospective subsampling patterns on the Cartesian grid:

## Cartesian Subsampling

- **Rectilinear:** Achieved by including some and omitting other horizontal (phase encoding direction) lines on the Cartesian grid. For the autocalibration region we use a number of  $r_{\text{acs}} \cdot n_y$  lines, where  $0 < r_{\text{acs}} < 1$ . We used four distinct rectilinear sampling patterns:
  - Random (Figure 3(a)): Lines were included uniformly at random with possible overlap with the ACS lines.
  - Equispaced (Figure 3(b)): Lines were included with a fixed distancing that satisfied the desired acceleration.
  - Equispaced+ (Figure 3(c)) : Improved rectilinear equispaced pattern by exploiting the  $k$ -space symmetry [31].
  - Gaussian 1D (Figure 3(d)): Lines were drawn from the Gaussian distribution with mean  $\mu = \frac{n_y}{2}$  and standard deviation  $\sigma = 4 \cdot \sqrt{\mu}$ .
- **Variable Density Poisson Disk (VDPD, Figure 3(e)):** Combines both random sampling and denser center sampling. For our implementation we followed Bridson’s algorithm in [29], which is a fast algorithm of order  $\mathcal{O}(n)$ . Samples were drawn with a density  $\frac{1}{1+s \cdot |r|}$ , i.e. inversely proportional to the  $k$ -space radius  $r$  and a slope  $s$  which were determined by the prescribed acceleration. For the autocalibration signal we fully-sampled a centered disk with a radius  $\frac{n_x \cdot n_y \cdot r_{\text{acs}}}{\pi}$ .
- **Gaussian 2D (Figure 3(f)):** Samples were drawn from the Gaussian distribution with mean  $\mu = \frac{1}{2}(n_x, n_y)$  and covariance  $\Sigma = 4 \cdot \mathbf{I}_2 \cdot \sqrt{\mu}^T$ .  
Code for VDPD and Gaussian 2D schemes was implemented in Cython for fast and efficient sampling.

**Simulated non-Cartesian Subsampling** To simulate non-Cartesian subsampling, we applied the CIRCular Cartesian UnderSampling (CIRCUS) [30] technique to produce the following retrospective subsampling patterns for Cartesian data:

- **Radial (Figure 3(g)):** Simulates radial subsampling on the Cartesian grid.
- **Spiral (Figure 3(h)):** Simulates spiral subsampling on the Cartesian grid.

For randomization CIRCUS’ offset parameter as defined in [30] can be set to produce random radial and spiral patterns. CIRCUS was modified to output masks by specifying the acceleration factor. Note that in contrast to the rest of the subsampling patterns above, for the non-Cartesian case we did not sample the ACS region exclusively, as these patterns already fully-sample a great portion of the  $k$ -space center. Therefore, for the ACS subsampling mask  $\mathbf{U}_{\text{acs}}$  we calculated the largest sampled centered disk from  $\mathbf{U}$ .

## 3.2 Deep MRI-reconstruction Model Architecture

### 3.2.1 The Recurrent Variational Network

To compare and evaluate the aforementioned subsampling techniques we employed a DL-based reconstruction network, namely the Recurrent Variational Network [10] (RecurrentVarNet). The RecurrentVarNet is a DL-based inverse problem solver previously applied on the task of Accelerated MRI Reconstruction [10] with state-of-the-art performance (MC-MRI reconstruction challenge winning solution [32]). It iteratively solves the gradient descent scheme in the measurements domain as portrayed by Eq. 19 using convolutional recurrent neural networks (ConvRNNs) as a regularizer. The RecurrentVarNet takes subsampled multi-coil  $k$ -space as input and outputs a prediction of the fully-sampled multi-coil  $k$ -space measurements. It comprises of three main modules:

- **Recurrent Variational Block (RecurrentVarNet Block).** The RecurrentVarNet consists of  $T$  RecurrentVarNet Blocks which are the main blocks of the RecurrentVarNet each responsible for performing an unrolled gradient descent optimization time-step as in Eq. 19 by replacing  $\mathcal{H}_{\theta_t}$  with a recurrent unit denoted as  $\text{RNN}_{\theta_t}$ :

$$\begin{aligned} \mathbf{w}_t, \mathbf{h}_{t+1} &= \text{RNN}_{\theta_{t+1}} \left( \mathcal{R}_S \circ \mathcal{F}^{-1}(\mathbf{y}_t), \mathbf{h}_t \right), \\ \mathbf{y}_{t+1} &= \mathbf{y}_t - \alpha_{t+1} \mathbf{U}(\mathbf{y}_t - \tilde{\mathbf{y}}) + \mathcal{F} \circ \mathcal{E}_S(\mathbf{w}_t), \\ \mathbf{y}_0 &= \tilde{\mathbf{y}}, \quad t = 0, \dots, T-1. \end{aligned} \tag{20}$$

Each  $\text{RNN}_{\theta_t}$  is consisted of a convolutional layer (Conv) with a  $5 \times 5$  kernel followed by  $n_l$  cascades of alternating Convs with a  $3 \times 3$  kernel and convolutional gated recurrent units (ConvGRUs). A rectified linear unit is applied after each Conv excluding the last.  $\text{RNN}_{\theta_t}$  takes as input intermediate quantities of the image projection of the refined  $k$ -space  $\mathcal{R}_S \circ \mathcal{F}^{-1}(\mathbf{y}_{t-1})$  and the hidden state  $\mathbf{h}_{t-1}$  from the previous time-step.

- **Recurrent State Initializer (RSI).** It produces an initialization for the first hidden state  $\mathbf{h}_0$  to be used by  $\text{RNN}_{\theta_1}$  provided as input the SENSE reconstruction of the image projection of  $\mathbf{y}_0$ :

$$\mathbf{h}_0 = \text{RSI}\left(\text{SENSE}(\mathcal{F}^{-1}(\mathbf{y}_0))\right). \quad (21)$$

- **Sensitivity Estimation - Refinement (SER).** The RecurrentVarNet for Accelerated MRI Reconstruction also estimates at each iteration the coil sensitivity maps as in Eq. 10 and refines them using a U-Net [33] with trainable parameters  $\psi$  denoted as  $\mathcal{S}_\psi$ :

$$\mathbf{S} = \text{SER}(\tilde{\mathbf{S}}) : \quad \mathbf{S}^k = \mathcal{S}_\psi(\tilde{\mathbf{S}}^k), \quad k = 1, \dots, n_c. \quad (22)$$

### 3.3 Experimental Setup

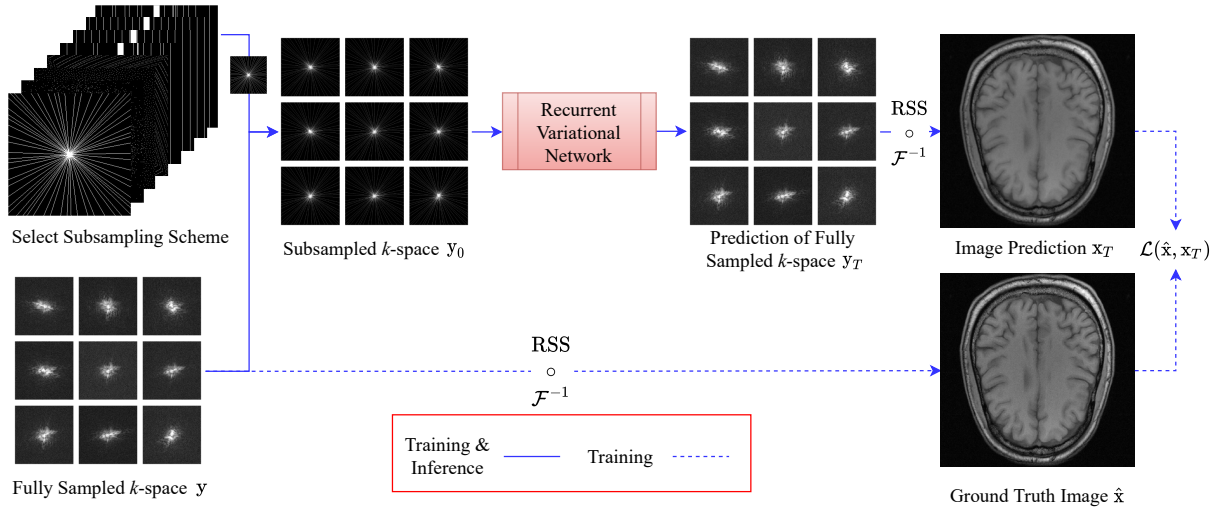


Figure 4: Experiments Pipeline: For each subsampling scheme (e.g. here: radial) the fully-sampled multi-coil  $k$ -space is retrospectively subsampled and used as input to a RecurrentVarNet which outputs a prediction of the fully-sampled  $k$ -space. The predicted  $\mathbf{x}_T$  and ground truth  $\hat{\mathbf{x}}$  images are produced by applying the  $\text{RSS} \circ \mathcal{F}^{-1}$  operator onto  $\mathbf{y}_T$  and  $\mathbf{y}$ , respectively. During training, the loss  $\mathcal{L}$  is calculated using  $\mathbf{x}_T$  and  $\hat{\mathbf{x}}$ .

To perform our experiments, we retrospectively subsampled the fully-sampled  $k$ -space data by generating subsampling masks as introduced in Section 3.1. We carried out two classes of experiments: Scheme-specific and Multi-scheme. An overview of our experimental setup is illustrated in Figure 4.

#### 3.3.1 Scheme-specific Setup

To compare the individual subsampling patterns and demonstrate their effect on the quality of DL-based reconstruction, we first performed experiments in a scheme-specific setting: for each dataset-pattern pair we ran individual experiments by training and evaluating (twenty-four) distinct RecurrentVarNets (with the same choice of hyper-parameters as outlined in Section 3.3.4).

#### 3.3.2 Multi-scheme Setup

In the multi-scheme setting, our goal was twofold: Firstly, we aimed to investigate further the effect of each subsampling scheme on the quality of DL-based reconstruction. Secondly and most importantly, we wanted to assess whether or not a DL-based model trained in a multi-scheme fashion (i.e. training measurements subsampled with multiple subsampling patterns) demonstrated higher reconstruction performance compared to being trained in a scheme-specific fashion (as in Section 3.3.1). Therefore, for each dataset a RecurrentVarNet was trained on data arbitrarily subsampled with any of the presented subsampling schemes in Section 3.1 and evaluated on all of them.

### 3.3.3 Subsampling

In both, scheme-specific and multi-scheme settings, throughout the training phase, subsampling masks were generated with an acceleration factor of  $R = 2, 4$  or  $8$ , and were retrospectively applied onto the fully-sampled data. At validation and testing times, data were 2-fold, 4-fold, and 8-fold retrospectively subsampled.

For the Cartesian masks we set  $r_{\text{acs}} = 0.16, 0.08, 0.04$  for  $R = 2, 4$  or  $8$ , respectively.

Note that for all experiments, subsampling masks during training were randomly generated to maximize the amount of data that each model saw, while for validation and testing they were predetermined. Additionally, the same subsampling mask was applied to all slices of each volume during validation and testing. It should also be highlighted that all individual coil data of each sample were subsampled with the same subsampling mask as this reflected clinical subsampling.

### 3.3.4 Model Implementation Details

**Hyper-parameter Choice** For the RecurrentVarNets we used  $T = 8$  time-steps. For each RecurrentVarNet Block we used  $n_l = 4$  alternating cascades and for the number of filters in each Conv and hidden size in each ConvGRU we chose  $n_f = 256$  channels. For the implementation of the RSI and SER modules we picked the same choice of hyper-parameters as the original paper [10].

**Training & Optimization Details** For training and optimization we utilized PyTorch [34]. All components of the Recurrent Variational Network were trained end-to-end and optimization was performed utilizing the Adam algorithm with coefficients  $(\beta_1, \beta_2) = (0.9, 0.999)$ , stability parameter  $\epsilon = 1 \times 10^{-8}$  and no weight decay.

Experiments were performed utilizing NVIDIA RTX A6000, Quadro RTX 8000, or A100 GPUs. Models were trained to convergence with a batch size of 1 slice multi-coil  $k$ -space data. The total number of trainable parameters for each model amounted to approximately 27,626k.

**Training Loss Function** At each training iteration each model was fed with subsampled multi-coil  $k$ -space measurements  $\tilde{\mathbf{y}}$  and produced a prediction  $\mathbf{y}_T$  of the fully-sampled reference  $k$ -space  $\mathbf{y}$ . Loss was computed in the image domain using  $\mathbf{x}_T = \text{RSS} \circ \mathcal{F}^{-1}(\mathbf{y}_T)$  as the image prediction and  $\hat{\mathbf{x}} = \text{RSS} \circ \mathcal{F}^{-1}(\mathbf{y})$  as the image reference.

As a loss function we used a combination of the mean average error (MAE) loss  $\mathcal{L}_{\text{MAE}}$  and the structural similarity index measure (SSIM) loss  $\mathcal{L}_{\text{SSIM}}$ :

$$\begin{aligned} \mathcal{L}(\hat{\mathbf{x}}, \mathbf{x}_T) &= \mathcal{L}_{\text{MAE}}(\hat{\mathbf{x}}, \mathbf{x}_T) + \mathcal{L}_{\text{SSIM}}(\hat{\mathbf{x}}, \mathbf{x}_T) \\ &= \|\hat{\mathbf{x}} - \mathbf{x}_T\|_1 + (1 - \text{SSIM}(\hat{\mathbf{x}}, \mathbf{x}_T)), \end{aligned} \quad (23)$$

where SSIM is defined in Section 3.3.6.

### 3.3.5 Datasets

To perform our experiments we employed three open source datasets, the fastMRI knee and brain datasets [35] which are to-date the largest publicly available MRI datasets, and the Calgary-Campinas (CC) brain dataset which was released as part of the Multi-Coil MRI Reconstruction Challenge [32]. All datasets consist of raw three dimensional  $k$ -space volumes which are multi-coil and fully-sampled conventional Cartesian acquisitions. The acquisition parameters and the splitting ratios we opted for in our experiments are summarized in Supporting Information Table S1.

### 3.3.6 Quality Analysis

**Metrics** To analyse and compare our results we employed three evaluation metrics commonly used in image processing. Assuming  $\mathbf{u} \in \mathbb{R}^n$  was the ground truth image and  $\mathbf{v} \in \mathbb{R}^n$  the prediction, they are defined as follows:

#### A) Structural Similarity Index Measure (SSIM)

$$\text{SSIM}(\mathbf{u}, \mathbf{v}) = \frac{1}{M} \sum_{i=1}^M \frac{(2\mu_{\mathbf{u}_i}\mu_{\mathbf{v}_i} + c_1)(2\sigma_{\mathbf{u}_i\mathbf{v}_i} + c_2)}{(\mu_{\mathbf{u}_i}^2 + \mu_{\mathbf{v}_i}^2 + c_1)(\sigma_{\mathbf{u}_i}^2 + \sigma_{\mathbf{v}_i}^2 + c_2)}, \quad (24)$$

where  $\mathbf{u}_i, \mathbf{v}_i, i = 1, \dots, M$  are image windows of size  $(w_x, w_y) = (7, 7)$  from  $\mathbf{u}$  and  $\mathbf{v}$ , respectively. The numbers  $\mu_{\mathbf{u}_i}, \mu_{\mathbf{v}_i}, \sigma_{\mathbf{u}_i}$  and  $\sigma_{\mathbf{v}_i}$  denote the means and standard deviations of each image window and  $\sigma_{\mathbf{u}_i\mathbf{v}_i}$  denotes the covariance between  $\mathbf{u}_i$  and  $\mathbf{v}_i$ . The constants  $c_1 = 0.01$  and  $c_2 = 0.03$  are used for numerical stability.

**B) Peak Signal-to-Noise Ratio (pSNR)**

$$\text{pSNR}(\mathbf{u}, \mathbf{v}) = 20 \log_{10} \left( \frac{\max(\mathbf{u})}{\sqrt{\frac{1}{n} \sum_i^n (\mathbf{u}_i - \mathbf{v}_i)^2}} \right) \quad (25)$$

**C) Normalized Mean Squared Error (NMSE)**

$$\text{NMSE}(\mathbf{u}, \mathbf{v}) = \frac{\|\mathbf{u} - \mathbf{v}\|_2^2}{\|\mathbf{u}\|_2^2} = \frac{\sum_i^n (\mathbf{u}_i - \mathbf{v}_i)^2}{\sum_i^n \mathbf{u}_i^2} \quad (26)$$

Note that the higher the computed SSIM and pSNR values are, the higher the quality of the reconstruction is, whereas for the NMSE values, the lower they are the lower the quality of the reconstruction is. Reported values for SSIM and NMSE are multiplied by 100 and 1000, respectively.

**3.3.7 Significance Tests**

To perform significance tests we used the Almost Stochastic Order (ASO) test [36, 37] with a 95% confidence level ( $\alpha = 0.05$ ). Each ASO test outputs a violation error  $\epsilon_{\min}$  which denotes the degree to which the hypothesis that "method A is always better than method B" is being violated. If  $\epsilon_{\min} \leq 0.5$  one can claim that A is better than B, and otherwise if  $\epsilon_{\min} > 0.5$ .

**4 Results**

To obtain our results, data preparation, retrospective subsampling generation, and model training we used the Deep Image Reconstruction Toolkit (DIRECT) [38].

**4.1 Scheme-specific Setup Results**

Figure 5 illustrates the quantitative metrics computed on the test sets in the form of violin-plots. The average metrics are reported in Supporting Information Table S2. Additionally, for visual assessment, in Figure 6, Figure 7, and Supporting Information Figure S1 we present example reconstructions of a test sample from each dataset using all methods along with ground truths and the retrospective subsampling mask used in each scenario.

**4.1.1 Cartesian**

**Rectilinear** Evidently, Figure 5 indicates that all models trained on rectilinearly subsampled measurements achieved comparable results when evaluated on the test sets subsampled with the respective rectilinear schemes. Moreover, although Gaussian 1D subsampling outperformed the rest of the rectilinear schemes in the case of both fastMRI datasets, the opposite was noted in the case of the CC dataset. This is also visible by the example reconstructions in Figures 6, 7, and Supporting Information Figure S1, especially for 8-fold acceleration.

**Non-Rectilinear** As Figure 5 and Supporting Information Table S2 indicate, models trained on data subsampled with either VDPD or Gaussian 2D schemes were the best-performing models when evaluated on the respective data. Additionally, they produced the higher average SSIM and pSNR and lower NMSE reconstructions for all combinations of datasets and acceleration factors.

**4.1.2 Non-Cartesian**

As shown in Figure 5 and Supporting Information Table S2, models trained and evaluated on simulated non-Cartesian (radially and spirally) subsampled data yielded similar performance to Cartesian non-rectilinear schemes. In general, spiral schemes outperformed radial schemes for all combinations of datasets and acceleration factors, though the difference in performance was minor.

**4.1.3 Comparisons**

Considering Figure 5, models trained on non-rectilinearly subsampled data, produced reconstructions of higher fidelity when evaluated on the respective test sets in comparison to models trained and evaluated on rectilinearly subsampled data for all datasets and acceleration factors. Models trained with VDPD-subsampled  $k$ -spaces obtained the best average quantitative evaluation results.



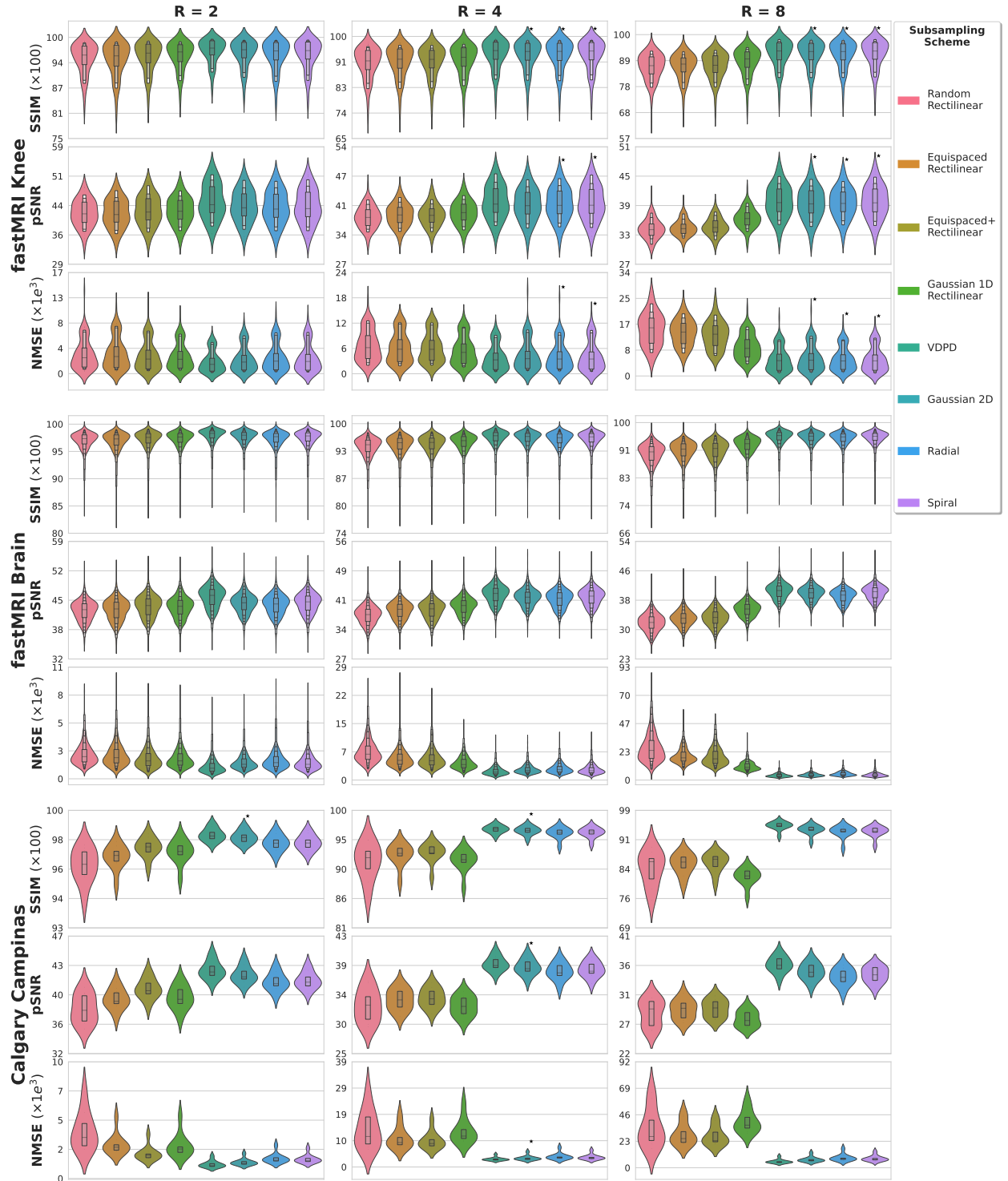


Figure 5: Scheme-specific experiments quantitative results on the test sets. For each dataset-subsampling scheme pair a distinct model was trained (in total 24 models). For each dataset-acceleration-metric combination, pair-wise ASO significance tests were performed between the average best performing (VDPD) and the rest schemes.  $\star$  indicates that VDPD was not found to be significantly better ( $\epsilon_{\min} > 0.5$ ). Average metrics are reported in Supporting Information Table S2.

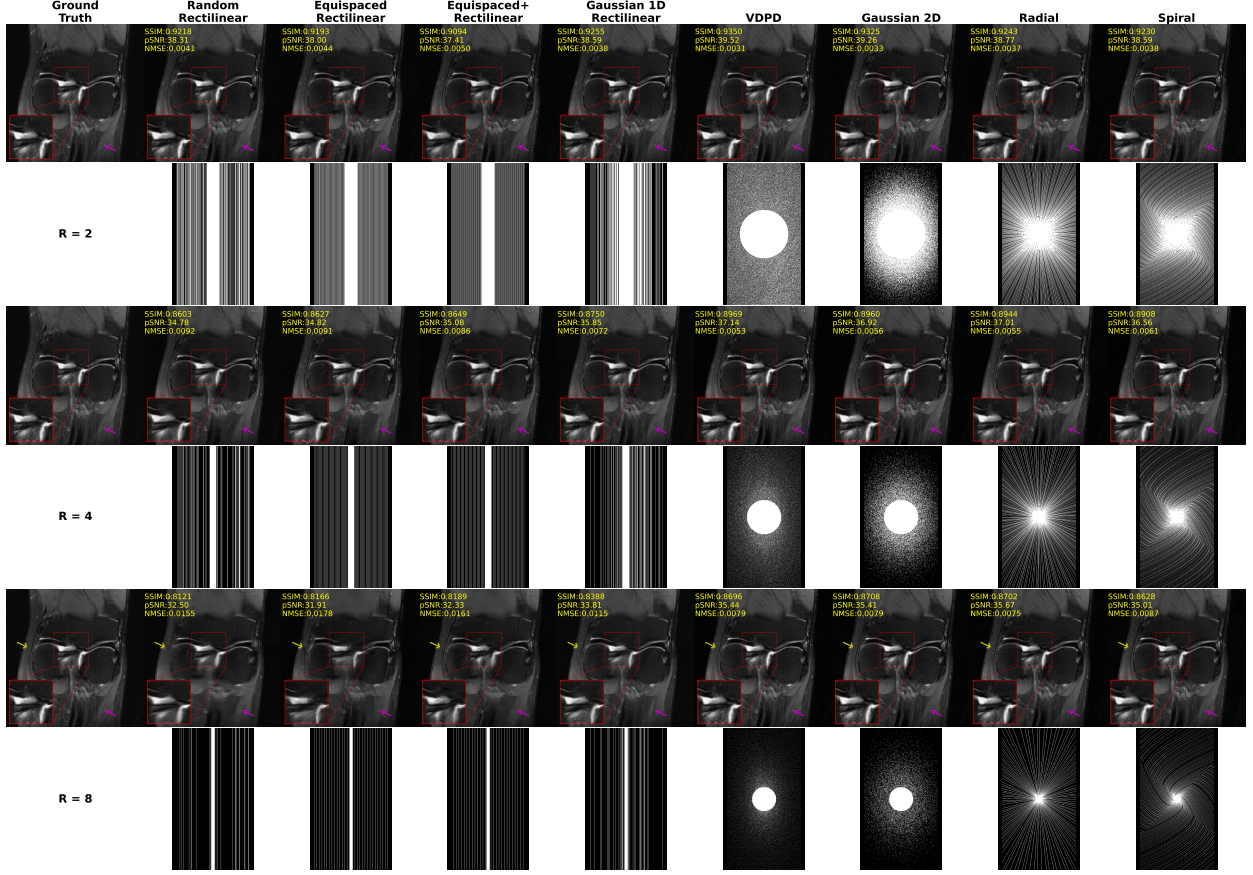


Figure 6: Representative reconstruction of a sample from the fastMRI knee test set obtained from the scheme-specific experiments. For the ground truth image the RSS method was applied on the fully sampled  $k$ -space. For each subsampling scheme, we retrospectively applied subsampling masks as shown in rows 2, 4, 6 (with accelerations factors of 2, 4, 8, respectively) onto the fully sampled  $k$ -space. Rows 1, 3, 5 illustrate the center-cropped RSS-reconstructed  $k$ -space output from each model. Quantitative metrics against the ground truth are inscribed on the top left of each reconstruction.

As apparent from Figure 6, Figure 7, and Supporting Information Figure S1, for high acceleration factors (4 or 8) models trained on rectilinear schemes were more prone to reconstructing images with more errors and artifacts, in contrast to non-Cartesian or non-rectilinear schemes. However, for  $R = 2$  all models evaluated closely.

## 4.2 Multi-scheme Setup Results

Figure 8 reports the quantitative evaluation results on the test sets in the multi-scheme setup and Supporting Information Table S3 the corresponding average metrics. We observe that, similarly to the results of Section 4.1, reconstructions of non-rectilinearly subsampled measurements produced better quantitative results compared to reconstructions of rectilinearly subsampled data. In addition, VDPD and Gaussian 2D-subsampled reconstructions were the highest performing in average.

For further investigation, in Supporting Information Figure S2, utilizing the results reported in Figure 8, we calculated the per-case difference in evaluation metrics change for each pattern using as reference the results obtained in the scheme-specific setup (Figure 5). We also report the average differences for rectilinear and non-rectilinear patterns in Table 1. Interestingly, models trained in the multi-scheme setting exemplified superior performance when evaluated on measurements subsampled with rectilinear schemes compared against the models trained on individual schemes when evaluated on the same data. In particular, in the case of rectilinear schemes, noticeable improvements (SSIM/pSNR increase, NMSE decrease) on the reconstruction performance were remarked for all datasets and acceleration factors, whilst for non-rectilinear patterns no change or minor deterioration was observed.

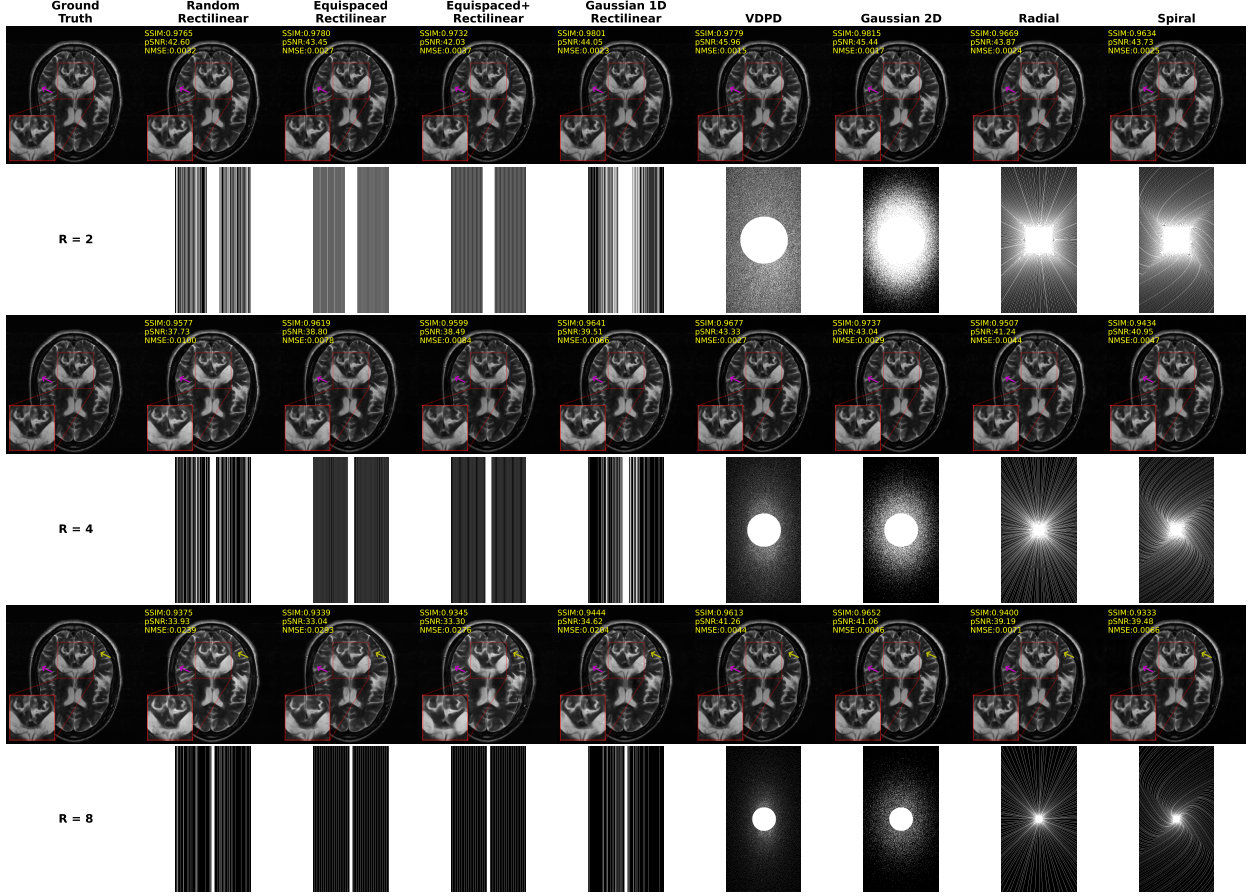


Figure 7: Representative reconstruction of a T2-weighted sample from the fastMRI brain test set obtained from the scheme-specific experiments. For the ground truth image the RSS method was applied on the fully sampled  $k$ -space. For each subsampling scheme, we retrospectively applied subsampling masks as shown in rows 2, 4, 6 (with accelerations factors of 2, 4, 8, respectively) onto the fully sampled  $k$ -space. Rows 1, 3, 5 illustrate the center-cropped RSS-reconstructed  $k$ -space output from each model. Quantitative metrics against the ground truth are inscribed on the top left of each reconstruction.

In Figure 9 and Supporting Information Figure S3 we plot representative reconstructions predicted from rectilinearly-subsampled data obtained from both, the scheme-specific and multi-scheme setups. By visual investigation, we notice that in the latter reconstructed images were more faithful.

### 4.3 Results - Model Dependence

To demonstrate that the results presented above did not rely on the choice of the model architecture we further experimented by employing an additional state-of-the-art deep-MRI reconstruction network: the Recurrent Inference Machine (RIM). More precisely, we repeated the scheme-specific experiments on the CC dataset by replacing the RecurrentVarNet with a RIM. The choice of hyper-parameters for each RIM was identical as in [19].

In Supporting Information Figure S4 and Table S4 are presented the quantitative metrics for our RIM experiments. Results were on par with the findings of our original experiments, suggesting that our conclusions were not dependent on the choice of DL architecture.

## 5 Discussion

In this work we investigated and compared various retrospective  $k$ -space subsampling patterns and we experimentally studied their effect on the quality of DL-based reconstructions. Since the data we utilized in our studies were Cartesian fully-sampled acquisitions, we retrospectively generated subsampling masks on the Cartesian grid as demonstrated in

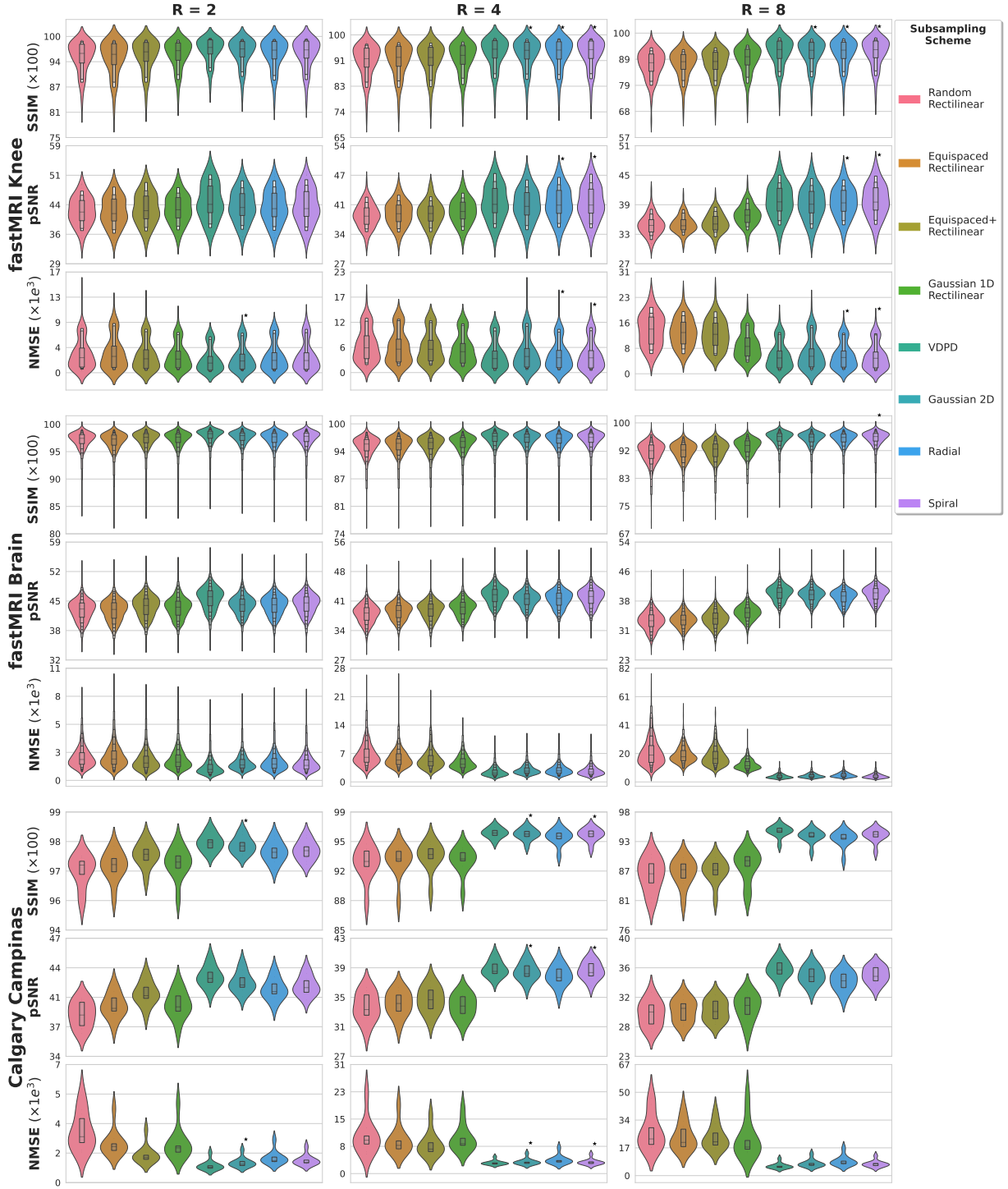


Figure 8: Multi-scheme experiments quantitative results on the test sets. For each dataset-acceleration-metric combination, pair-wise ASO significance tests were performed between the average best performing (VDPD) and the rest schemes.  $\star$  indicates that VDPD was not found to be significantly better ( $\epsilon_{\min} > 0.5$ ). Average metrics are reported in Supporting Information Table S3.

Section 3.1, simulating prospective Cartesian or non-Cartesian accelerated acquisitions. In particular, we generated four Cartesian rectilinear schemes (random, equispaced, equispaced with symmetry correction, Gaussian), non-rectilinear Cartesian schemes (Variable Density Poisson-disk and Gaussian 2D), and simulated (non-Cartesian) radial and spiral schemes.

Our experiments consisted of utilizing a state-of-the-art DL-based accelerated MRI reconstruction method - the Recurrent Variational Network. Although choosing the optimal DL-based MRI reconstruction algorithm was out of the scope of this project, it is important to note that other DL-based models do exist with similar performance. However, the RecurrentVarNet was chosen as it has previously shown to produce high-fidelity reconstructions and outperform other models in reconstruction performance. Additionally, to demonstrate that the results were not model-dependent, the scheme-specific experiments on the CC dataset were repeated using the RIM model which produced on-par results.

Experiments were performed under two setups: scheme-specific and multi-scheme setups. In the scheme-specific settings, we trained individual models on data retrospectively subsampled with individual subsampling patterns applying various acceleration factors. Quantitative and qualitative results demonstrated that the models trained on conventional rectilinear schemes, in contrast to other schemes, produced lower quality reconstructions with more artifacts especially for higher acceleration factors (4 or 8). This can be attributed to the fact that non-rectilinear Cartesian such as the VDPD or the Gaussian 2D, and non-Cartesian patterns such as the radial or spiral, allow for more incoherent sampling. This means that these schemes result in a more randomized and less correlated distribution of samples, reducing the dependence of the reconstruction quality on any specific pattern of missing data. Additionally, these schemes allow for center oversampling, which contains information such as contrast and the general shape of the reconstruction.

In the multi-scheme setup, unified models were trained on all distributions of subsampled patterns. Although quantitative results were on par with the results of our scheme-specific experiments, we observed noticeable improvements (compared to the scheme-specific results) of the reconstruction inference performance for rectilinearly subsampled measurements. Additionally, the violin-plots in Figure 5 and Figure 8 show that for most dataset-metric-acceleration combinations quantitative results for the four rectilinear and the four non-rectilinear schemes formed similar metric distributions and were with similar numbers of outliers, suggesting that results were also case-dependent.

Even though comparing prospective acquisition speeds was out of the scope of this project, we provide a brief discussion. While the reconstruction performance of Cartesian rectilinearly subsampled data was inferior to Cartesian non-rectilinear, someone could argue about the trade-off between acquisition speed and quality, as MRI scanners can perform rectilinear sampling in fast acquisition times [1], while strategies such as VDPD or Gaussian 2D can be slower due to physical limitations. For instance, in the prospective case these strategies may require large gradient switches in the MRI scanner due to the enlarged  $k$ -space spacing which can cause extended times due to hardware constraints, whilst in the retrospective settings, efficient algorithms are used to pick the samples. On the other hand, our results indicated that synthesized radial or spiral schemes on the Cartesian grid using the CIRCUS method provided similar performance to VDPD and Gaussian 2D schemes. In the original paper [30], the authors state that their method improved sampling efficiency over VDPD while maintaining the reconstruction performance in the prospective case.

However, prospective non-Cartesian sampling trajectories do not sample on a Cartesian grid, and therefore samples closer to the center are more densely placed, and more scattered far off. As a result of this non-uniformity, for the application of the FFT a gridding and inverse-gridding process [39] is required to place them onto a Cartesian grid accumulating additional computation times. Note that gridding can be replaced with the application of the non-uniform FFT (NUFFT) [40].

The main limitation of this study is the fact that experiments were performed retrospectively. In our future work, we will repeat our experiments using prospectively subsampled data with the different schemes we employed in this study

Table 1: Scheme-specific-Multi-scheme experiments performance average percentage difference. Percentages were acquired by averaging the per-case differences (as calculated and illustrated in Supporting Information Figure S2) for all dataset-scheme type (rectilinear or non-rectilinear) combinations.

Dataset	Type of Subsampling Scheme	Acceleration Factor ( $R$ )								
		2			4			8		
		SSIM	pSNR	NMSE	SSIM	pSNR	NMSE	SSIM	pSNR	NMSE
FastMRI Knee	Rectilinear	0.1%	0.5%	-0.7%	0.3%	0.8%	-3.2%	0.7%	1.4%	-9.4%
	Non-rectilinear	0.0%	-0.3%	5.2%	0.0%	-0.2%	4.2%	0.0%	-0.1%	3.1%
FastMRI Brain	Rectilinear	0.0%	0.3%	-2.6%	0.1%	0.2%	-1.6%	0.3%	0.7%	-4.8%
	Non-rectilinear	0.0%	-0.2%	1.8%	0.0%	-0.1%	0.7%	0.0%	0.0%	-0.6%
Calgary Campinas	Rectilinear	0.3%	1.6%	-13.9%	1.2%	2.7%	-18.5%	3.7%	5.0%	-26.0%
	Non-rectilinear	0.0%	0.1%	-1.4%	0.0%	0.0%	0.3%	0.0%	0.0%	0.2%



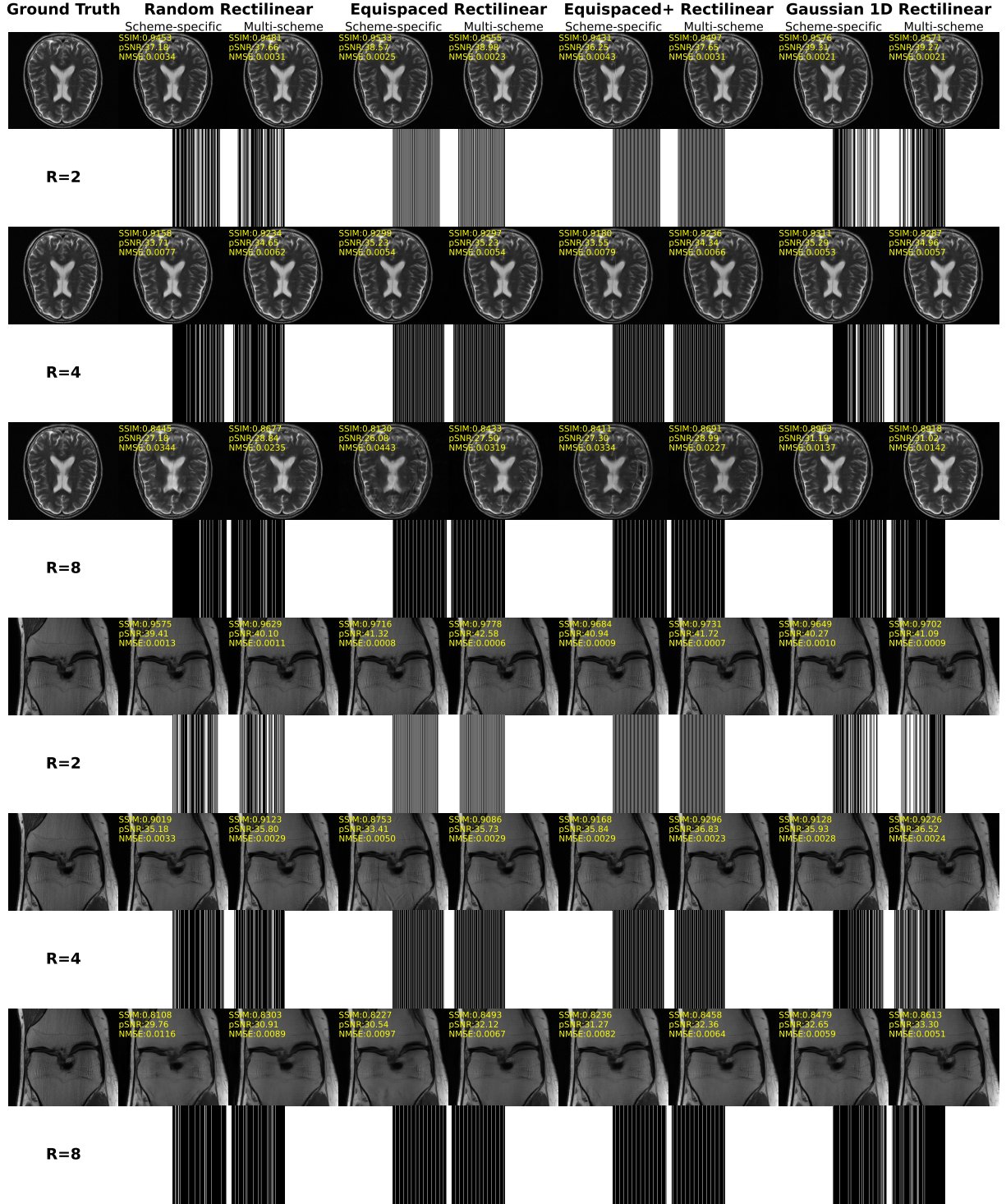


Figure 9: Scheme-specific vs multi-scheme setup visual comparison: Representative reconstructions of two samples from the fastMRI dataset. Measurements were subsampled with the four rectilinear schemes obtained from the scheme-specific and multi-scheme experiments for three acceleration factors.

in order to determine the extend to which our findings hold true in prospective settings. To that end it will be necessary to apply one of the methods discussed in the previous paragraph to handle non-Cartesian data in order to incorporate it into our deep learning pipeline and match the multi-scheme framework used in this study.

## 6 Conclusion

In summary, we experimentally showed that DL-based accelerated MRI reconstruction methods trained on data retrospectively subsampled with Cartesian non-rectilinear or simulated non-Cartesian trajectories, compared against Cartesian rectilinear trajectories, can produce more robust and truthful reconstructions allowing for high acceleration factors.

## Acknowledgements

This work was funded by an institutional grant from the Dutch Cancer Society and the Dutch Ministry of Health, Welfare and Sport.

## References

- [1] Michael Lustig, David Donoho, and John M. Pauly. Sparse mri: The application of compressed sensing for rapid mr imaging. *Magnetic Resonance in Medicine*, 58(6):1182–1195, 2007.
- [2] D.L. Donoho. Compressed sensing. *IEEE Transactions on Information Theory*, 52(4):1289–1306, 2006.
- [3] Emmanuel J. Candès, Justin K. Romberg, and Terence Tao. Stable signal recovery from incomplete and inaccurate measurements. *Communications on Pure and Applied Mathematics*, 59(8):1207–1223, 2006.
- [4] E.J. Candès, J. Romberg, and T. Tao. Robust uncertainty principles: exact signal reconstruction from highly incomplete frequency information. *IEEE Transactions on Information Theory*, 52(2):489–509, 2006.
- [5] C.E. Shannon. Communication in the presence of noise. *Proceedings of the IRE*, 37(1):10–21, 1949.
- [6] Shiqian Ma, Wotao Yin, Yin Zhang, and Amit Chakraborty. An efficient algorithm for compressed mr imaging using total variation and wavelets. In *2008 IEEE Conference on Computer Vision and Pattern Recognition*, pages 1–8, 2008.
- [7] Michael Lustig and John M. Pauly. Spirit: Iterative self-consistent parallel imaging reconstruction from arbitrary k-space. *Magnetic Resonance in Medicine*, 64(2):457–471, jun 2010.
- [8] Mark A. Griswold, Peter M. Jakob, Robin M. Heidemann, Mathias Nittka, Vladimir Jellus, Jianmin Wang, Berthold Kiefer, and Axel Haase. Generalized autocalibrating partially parallel acquisitions (GRAPPA). *Magnetic Resonance in Medicine*, 47(6):1202–1210, jun 2002.
- [9] Klaas P. Pruessmann. Encoding and reconstruction in parallel mri. *NMR in Biomedicine*, 19(3):288–299, 2006.
- [10] George Yiasemis, Jan-Jakob Sonke, Clarisa Sánchez, and Jonas Teuwen. Recurrent variational network: A deep learning inverse problem solver applied to the task of accelerated mri reconstruction. In *Proceedings of the IEEE/CVF Conference on Computer Vision and Pattern Recognition (CVPR)*, pages 732–741, June 2022.
- [11] Anuroop Sriram, Jure Zbontar, Tullie Murrell, Aaron Defazio, C. Lawrence Zitnick, Nafissa Yakubova, Florian Knoll, and Patricia Johnson. End-to-end variational networks for accelerated mri reconstruction. In Anne L. Martel, Purang Abolmaesumi, Danail Stoyanov, Diana Mateus, Maria A. Zuluaga, S. Kevin Zhou, Daniel Racoceanu, and Leo Joskowicz, editors, *Medical Image Computing and Computer Assisted Intervention – MICCAI 2020*, pages 64–73, Cham, 2020. Springer International Publishing.
- [12] Yohan Jun, Hyungseob Shin, Taejoon Eo, and Dosik Hwang. Joint deep model-based mr image and coil sensitivity reconstruction network (joint-icnet) for fast mri. In *2021 IEEE/CVF Conference on Computer Vision and Pattern Recognition (CVPR)*, pages 5266–5275, 2021.
- [13] Patrick Putzky and Max Welling. Recurrent inference machines for solving inverse problems, 2017.
- [14] Kerstin Hammernik, Teresa Klatzer, Erich Kobler, Michael P. Recht, Daniel K. Sodickson, Thomas Pock, and Florian Knoll. Learning a variational network for reconstruction of accelerated mri data. *Magnetic Resonance in Medicine*, 79(6):3055–3071, 2018.
- [15] Taejoon Eo, Yohan Jun, Taeseong Kim, Jinseong Jang, Ho-Joon Lee, and Dosik Hwang. Kiki-net: cross-domain convolutional neural networks for reconstructing undersampled magnetic resonance images. *Magnetic Resonance in Medicine*, 80(5):2188–2201, apr 2018.
- [16] Anuroop Sriram, Jure Zbontar, Tullie Murrell, C. Lawrence Zitnick, Aaron Defazio, and Daniel K. Sodickson. Grappanet: Combining parallel imaging with deep learning for multi-coil mri reconstruction. In *Proceedings of the IEEE/CVF Conference on Computer Vision and Pattern Recognition (CVPR)*, June 2020.

- [17] Roberto Souza, Mariana Bento, Nikita Nogovitsyn, Kevin J. Chung, Wallace Loos, R. Marc Lebel, and Richard Frayne. Dual-domain cascade of u-nets for multi-channel magnetic resonance image reconstruction. *Magnetic Resonance Imaging*, 71:140–153, sep 2020.
- [18] Li Feng, Robert Grimm, Kai Tobias Block, Hersh Chandarana, Sungheon Kim, Jian Xu, Leon Axel, Daniel K Sodickson, and Ricardo Otazo. Golden-angle radial sparse parallel MRI: combination of compressed sensing, parallel imaging, and golden-angle radial sampling for fast and flexible dynamic volumetric MRI. *Magn. Reson. Med.*, 72(3):707–717, September 2014.
- [19] George Yiasemis, Chaoping Zhang, Clara I. Sánchez, Jan-Jakob Sonke, and Jonas Teuwen. Deep MRI reconstruction with radial subsampling. In Wei Zhao and Lifeng Yu, editors, *Medical Imaging 2022: Physics of Medical Imaging*. SPIE, apr 2022.
- [20] Klaas P. Pruessmann, Markus Weiger, Markus B. Scheidegger, and Peter Boesiger. Sense: Sensitivity encoding for fast mri. *Magnetic Resonance in Medicine*, 42(5):952–962, 1999.
- [21] Angshul Majumdar and Rabab K. Ward. Iterative estimation of mri sensitivity maps and image based on sense reconstruction method (isense). *Concepts in Magnetic Resonance Part A*, 40A(6):269–280, 2012.
- [22] Martin Uecker, Peng Lai, Mark J Murphy, Patrick Virtue, Michael Elad, John M Pauly, Shreyas S Vasanaawala, and Michael Lustig. ESPIRiT—an eigenvalue approach to autocalibrating parallel MRI: where SENSE meets GRAPPA. *Magn. Reson. Med.*, 71(3):990–1001, March 2014.
- [23] Xiaofang Liu, Wenlong Xu, and Xiuzi Ye. The ill-posed problem and regularization in parallel magnetic resonance imaging. In *2009 3rd International Conference on Bioinformatics and Biomedical Engineering*, pages 1–4, 2009.
- [24] Martin Uecker. Parallel magnetic resonance imaging. arXiv, 2015.
- [25] E.Loli Piccolomini, F. Zama, G. Zanghirati, and A. Formiconi. Regularization methods in dynamic mri. *Applied Mathematics and Computation*, 132(2):325–339, 2002.
- [26] Fa-Hsuan Lin, Kenneth K. Kwong, John W. Belliveau, and Lawrence L. Wald. Parallel imaging reconstruction using automatic regularization. *Magnetic Resonance in Medicine*, 51(3):559–567, feb 2004.
- [27] Florian Knoll, Christian Clason, Kristian Bredies, Martin Uecker, and Rudolf Stollberger. Parallel imaging with nonlinear reconstruction using variational penalties. *Magnetic Resonance in Medicine*, 67(1):34–41, 2012.
- [28] Daniel K. Sodickson and Charles A. McKenzie. A generalized approach to parallel magnetic resonance imaging. *Medical Physics*, 28(8):1629–1643, aug 2001.
- [29] Robert Bridson. Fast poisson disk sampling in arbitrary dimensions. In *ACM SIGGRAPH 2007 Sketches*, SIGGRAPH ’07, page 22–es, New York, NY, USA, 2007. Association for Computing Machinery.
- [30] Jing Liu and David Saloner. Accelerated mri with circular cartesian undersampling (circus): a variable density cartesian sampling strategy for compressed sensing and parallel imaging. *Quantitative Imaging in Medicine and Surgery*, 4(1), 2014.
- [31] Aaron Defazio. Offset sampling improves deep learning based accelerated mri reconstructions by exploiting symmetry, 2019.
- [32] Youssef Beauferris, Jonas Teuwen, Dimitrios Karkaloulos, Nikita Moriakov, Matthan Caan, George Yiasemis, Livia Rodrigues, Alexandre Lopes, Helio Pedrini, Letícia Rittner, Maik Dannecker, Viktor Studenyak, Fabian Gröger, Devendra Vyas, Shahrooz Faghih-Roohi, Amrit Kumar Jethi, Jaya Chandra Raju, Mohanasankar Sivaprakasam, Mike Lasby, Nikita Nogovitsyn, Wallace Loos, Richard Frayne, and Roberto Souza. Multi-coil MRI reconstruction challenge—assessing brain MRI reconstruction models and their generalizability to varying coil configurations. *Frontiers in Neuroscience*, 16, jul 2022.
- [33] Olaf Ronneberger, Philipp Fischer, and Thomas Brox. U-net: Convolutional networks for biomedical image segmentation. In *Lecture Notes in Computer Science*, pages 234–241. Springer International Publishing, 2015.
- [34] Adam Paszke, Sam Gross, Francisco Massa, Adam Lerer, James Bradbury, Gregory Chanan, Trevor Killeen, Zeming Lin, Natalia Gimelshein, Luca Antiga, Alban Desmaison, Andreas Kopf, Edward Yang, Zachary DeVito, Martin Raison, Alykhan Tejani, Sasank Chilamkurthy, Benoit Steiner, Lu Fang, Junjie Bai, and Soumith Chintala. Pytorch: An imperative style, high-performance deep learning library. In *Advances in Neural Information Processing Systems 32*, pages 8024–8035. Curran Associates, Inc., 2019.
- [35] Jure Zbontar, Florian Knoll, Anuroop Sriram, Tullie Murrell, Zhengnan Huang, Matthew J. Muckley, Aaron Defazio, Ruben Stern, Patricia Johnson, Mary Bruno, Marc Parente, Krzysztof J. Geras, Joe Katsnelson, Hersh Chandarana, Zizhao Zhang, Michal Drozdal, Adriana Romero, Michael Rabbat, Pascal Vincent, Nafissa Yakubova, James Pinkerton, Duo Wang, Erich Owens, C. Lawrence Zitnick, Michael P. Recht, Daniel K. Sodickson, and Yvonne W. Lui. fastmri: An open dataset and benchmarks for accelerated mri, 2018.



- [36] Rotem Dror, Segev Shlomov, and Roi Reichart. Deep dominance - how to properly compare deep neural models. In *Proceedings of the 57th Annual Meeting of the Association for Computational Linguistics*, pages 2773–2785, Florence, Italy, July 2019. Association for Computational Linguistics.
- [37] Dennis Ulmer, Christian Hardmeier, and Jes Frellsen. deep-significance-easy and meaningful statistical significance testing in the age of neural networks. *arXiv preprint arXiv:2204.06815*, 2022.
- [38] George Yiasemis, Nikita Moriakov, Dimitrios Karkaloulos, Matthan Caan, and Jonas Teuwen. Direct: Deep image reconstruction toolkit, 2022.
- [39] J.I. Jackson, C.H. Meyer, D.G. Nishimura, and A. Macovski. Selection of a convolution function for fourier inversion using gridding (computerised tomography application). *IEEE Transactions on Medical Imaging*, 10(3):473–478, 1991.
- [40] Karsten Fourmont. Non-equispaced fast fourier transforms with applications to tomography. *Journal of Fourier Analysis and Applications*, 9(5):431–450, sep 2003.

## Supporting information

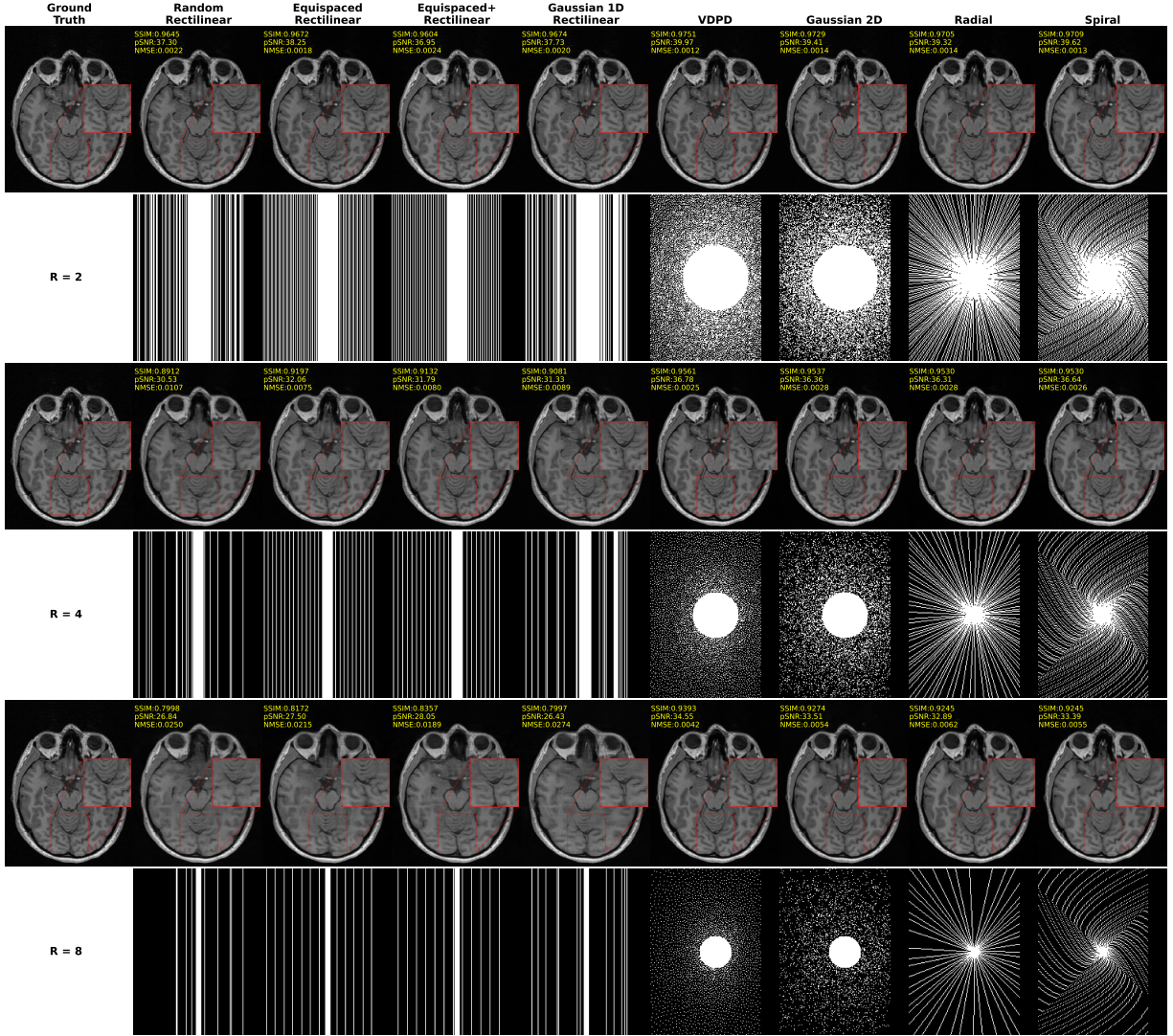


Figure S1 : Representative reconstruction of a sample from the Calgary Campinas test set obtained from the scheme-specific experiments. For the ground truth image the RSS method was applied on the fully sampled  $k$ -space. For each subsampling scheme, we retrospectively applied subsampling masks as shown in rows 2, 4, 6 (with accelerations factors of 2, 4, 8, respectively) onto the fully sampled  $k$ -space. Rows 1, 3, 5 illustrate the RSS reconstructed  $k$ -space output from each model. Quantitative metrics against the ground truth are inscribed on the top left of each reconstruction. Note that the right 15% portion of the  $k$ -space was not collected and therefore subsampling masks were zero-filled accordingly.

Table S1 : Acquisition parameters and experiment splits per dataset used in our experiments.

Dataset	fastMRI Knee	fastMRI Brain	Calgary Campinas
Field Strength	1.5T & 3.0T	1.5T & 3.0T	3.0T
Sequence	PD <sup>1</sup> with and without fat suppression	T1-w <sup>2</sup> , T1-w post contrast, T2-w, FLAIR	T1-w
Subjects	Healthy or Abnormality present	Healthy or Pathology present	Presumed healthy
Acquisition	Cartesian	Cartesian	Cartesian
Fully Sampled	Yes	Yes	Yes
Subsampling	Phase and slice encoding directions	Phase and slice encoding directions	Phase and slice encoding directions
Directions			
No. Coils	15	2 - 24	12
No. Volumes	1172	5846	67
No. Slices	41877	92574	10452
Split size	Training	4469 / 70748	40 / 6240
(No. volumes / Validation	100 / 3587	686 / 10880	14 / 2184
No. slices) Test	99 / 3548	691 / 10946	13 / 2028

Proton Density  
Weighted

Table S2 : Scheme-specific experiments average results on the test sets. Bold numbers indicate the best across subsampling schemes.

Dataset	Subsampling Scheme	Acceleration Factor ( $R$ )								
		2			4			8		
		SSIM	pSNR	NMSE	SSIM	pSNR	NMSE	SSIM	pSNR	NMSE
fastMRI Knee	Random Rect.	0.9482	41.79	0.0032	0.9099	38.04	0.0066	0.8594	34.48	0.0138
	Equispaced Rect.	0.9439	41.43	0.0037	0.9120	38.37	0.0062	0.8643	34.17	0.0142
	Equispaced+ Rect.	0.9449	41.77	0.0033	0.9129	38.48	0.0060	0.8658	34.23	0.0140
	Gaussian 1D	0.9533	42.39	0.0028	0.9187	39.07	0.0054	0.8862	36.16	0.0094
	VDPD	<b>0.9656</b>	<b>44.76</b>	<b>0.0020</b>	<b>0.9378</b>	<b>41.54</b>	<b>0.0037</b>	<b>0.9176</b>	<b>39.56</b>	<b>0.0053</b>
	Gaussian 2D	0.9594	43.53	0.0024	0.9347	40.86	0.0042	0.9164	39.21	0.0057
	Radial	0.9556	43.27	0.0026	0.9347	41.05	0.0040	0.9165	39.26	0.0054
fastMRI Brain	Spiral	0.9570	43.51	0.0026	0.9365	41.23	0.0040	0.9189	39.52	0.0054
	Random Rect.	0.9698	42.74	0.0024	0.9436	37.72	0.0075	0.9016	32.26	0.0266
	Equispaced Rect.	0.9720	43.69	0.0020	0.9495	38.97	0.0056	0.9121	33.53	0.0194
	Equispaced+ Rect.	0.9687	42.95	0.0023	0.9490	38.90	0.0056	0.9111	33.34	0.0198
	Gaussian 1D	0.9729	43.60	0.0020	0.9544	39.87	0.0045	0.9289	35.73	0.0114
	VDPD	<b>0.9794</b>	<b>45.90</b>	<b>0.0012</b>	<b>0.9664</b>	<b>42.82</b>	<b>0.0023</b>	<b>0.9545</b>	<b>40.56</b>	<b>0.0039</b>
	Gaussian 2D	0.9763	44.45	0.0016	0.9646	42.01	0.0028	0.9526	40.03	0.0043
Calgary Campinas	Radial	0.9730	44.06	0.0018	0.9615	41.70	0.0030	0.9503	39.27	0.0051
	Spiral	0.9745	44.50	0.0016	0.9635	42.14	0.0027	0.9526	40.14	0.0042
	Random Rect.	0.9634	37.86	0.0039	0.9139	32.61	0.0137	0.8387	28.53	0.0346
	Equispaced Rect.	0.9737	40.47	0.0021	0.9280	33.77	0.0100	0.8541	29.24	0.0276
	Equispaced+ Rect.	0.9682	39.13	0.0028	0.9249	33.49	0.0105	0.8495	29.06	0.0290
	Gaussian 1D	0.9713	39.34	0.0027	0.9158	32.53	0.0130	0.8174	27.59	0.0399
	VDPD	<b>0.9811</b>	<b>42.89</b>	<b>0.0012</b>	<b>0.9653</b>	<b>38.95</b>	<b>0.0029</b>	<b>0.9486</b>	<b>36.27</b>	<b>0.0055</b>
	Gaussian 2D	0.9798	42.27	0.0013	0.9633	38.47	0.0033	0.9384	35.13	0.0071
	Radial	0.9763	41.37	0.0017	0.9596	37.79	0.0039	0.9331	34.29	0.0087
	Spiral	0.9765	41.53	0.0016	0.9602	38.09	0.0036	0.9337	34.64	0.0080

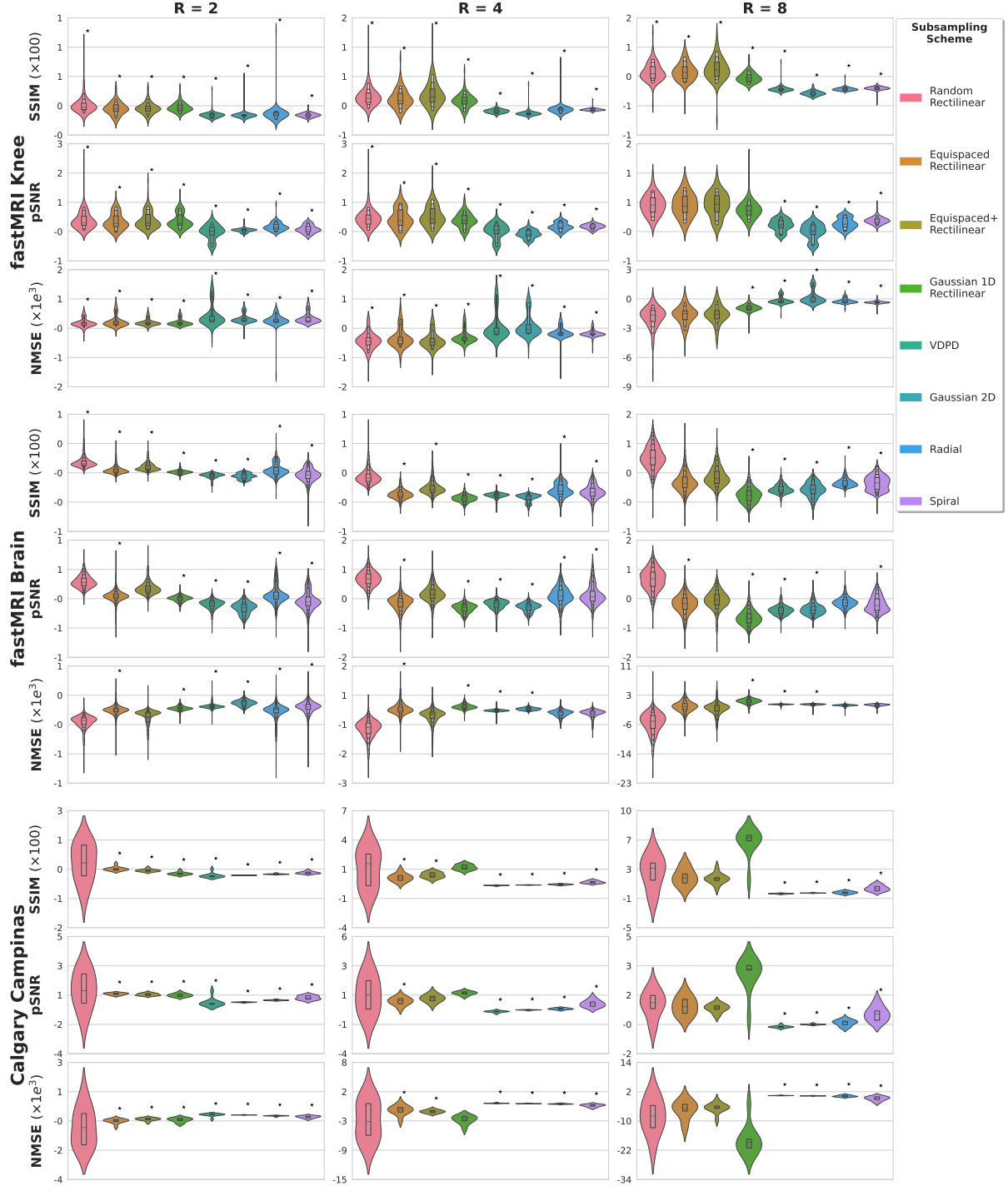


Figure S2 : Scheme-specific setup vs multi-scheme setup quantitative results comparison. Violin-plots illustrate the evaluation metric differences between the reconstructed output of the model trained on all subsampling schemes (multi-scheme) and the reconstructed output of the model trained on a single scheme (scheme-specific). Let  $\mathbf{y}$ ,  $\tilde{\mathbf{y}}^S$  be the fully-sampled and subsampled (with scheme  $S$ )  $k$ -space, respectively, and let  $\mathbf{u}$  be the RSS-reconstruction of  $\mathbf{y}$  (ground truth). Then, assuming that  $\mathbf{x}_M^S$  and  $\mathbf{x}_U^S$  are the image predictions output from the model trained on all subsampling schemes and the model trained on scheme  $S$ , respectively, we compute the difference  $m(\mathbf{u}, \mathbf{x}_M^S) - m(\mathbf{u}, \mathbf{x}_U^S)$ , for each metric  $m$ . Positive and negative differences in the case of SSIM/pSNR and NMSE, respectively, indicate that the multi-scheme model, performed better than then scheme-specific model. For each dataset-acceleration-metric combination, pair-wise ASO significance tests were performed between the multi-scheme and scheme-specific quantitative results.  $\star$  indicates that the performance difference was not found to be significant ( $\epsilon_{\min} > 0.5$ )

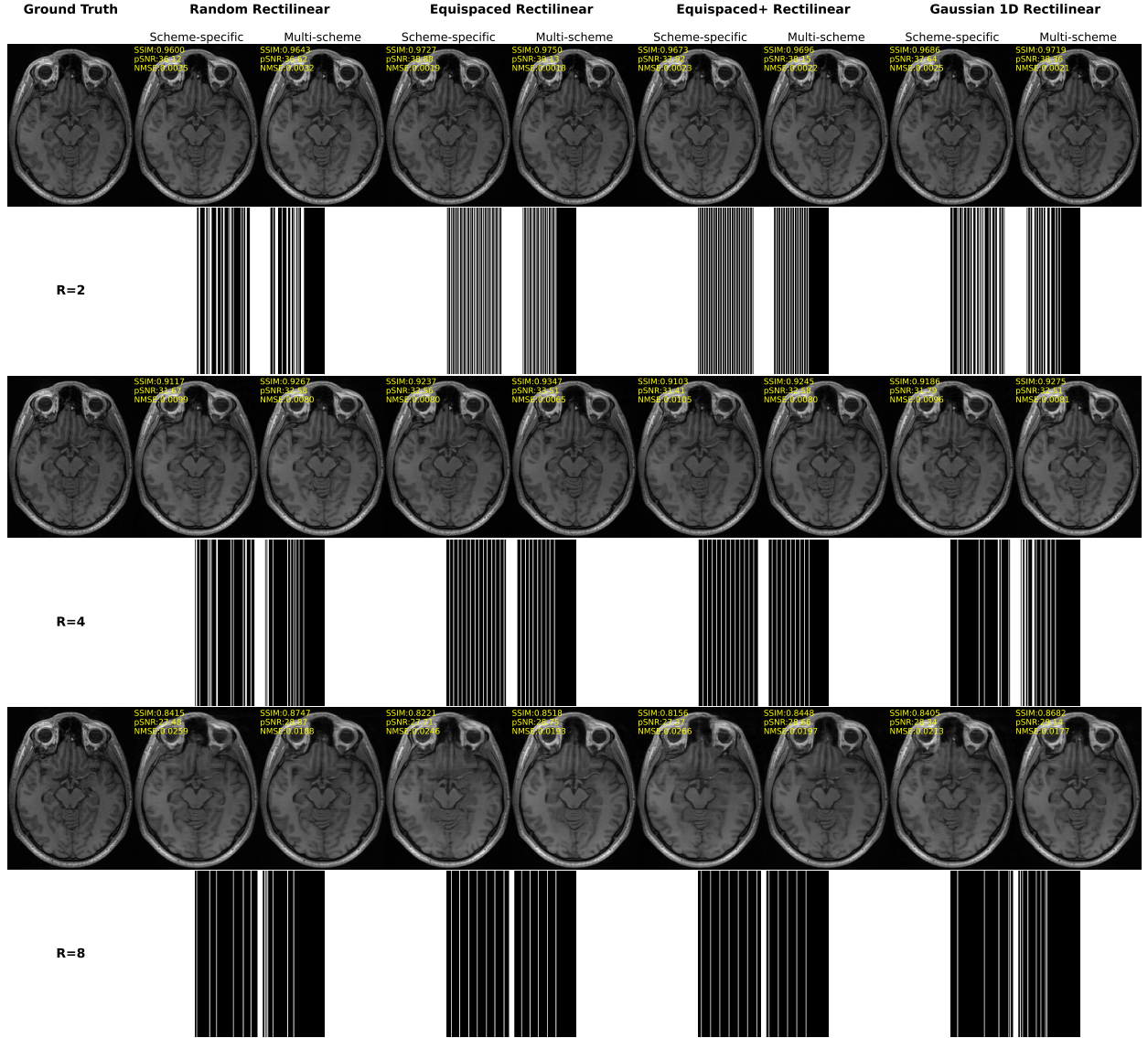


Figure S3 : Scheme-specific vs multi-scheme setups visual comparison. Representative reconstructions of a sample from the Calgary-Campinas dataset subsampled with the four rectilinear schemes obtained from the scheme-specific and multi-scheme experiments for three acceleration factors.

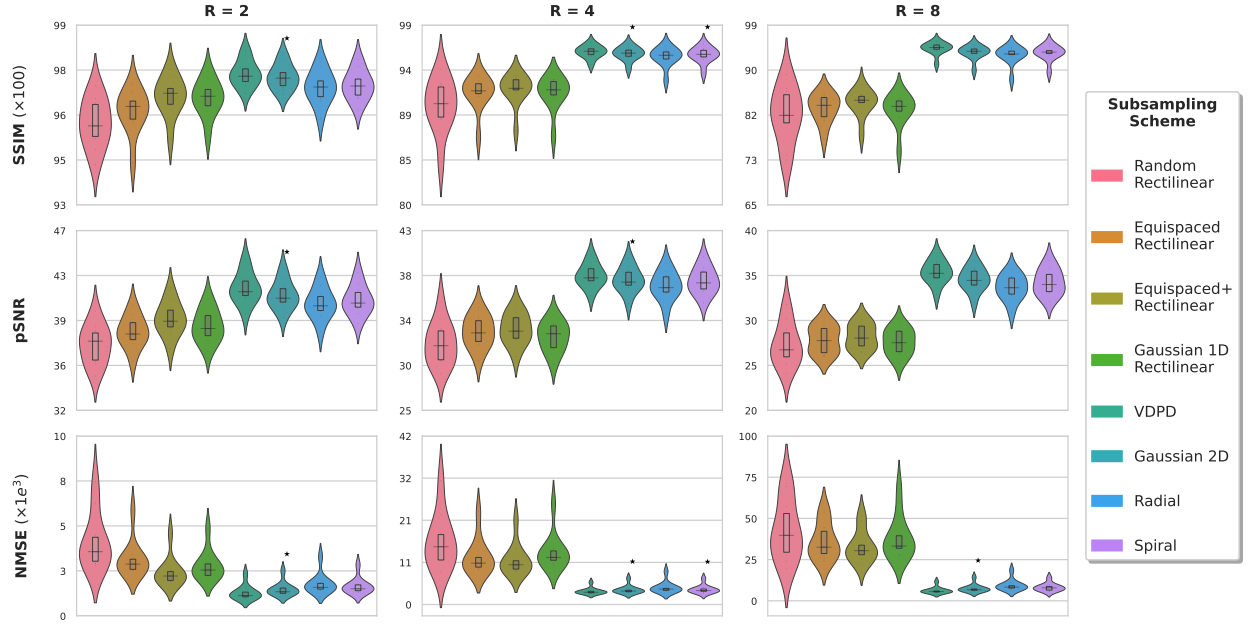


Figure S4 : Model dependence experiments quantitative results on the Calgary-Campinas dataset using RIMs instead of RecurrentVarNets. For each subsampling scheme a distinct RIM was trained (in total 8 models). All models were built with identical hyperparameters and were trained to convergence. In each case we picked to evaluate the best model based on the validation performance on the SSIM metric. For each acceleration-metric combination, pair-wise ASO significance tests were performed between the average best (VDPD) performing and the rest schemes. ★ indicates that VDPD was not found to be significantly better ( $\epsilon_{\min} > 0.5$ )

Table S3 : Multi-scheme experiments average results on the test sets. Bold numbers indicate the best across subsampling schemes.

Dataset	Subsampling Scheme	Acceleration Factor ( $R$ )								
		2			4			8		
		SSIM	pSNR	NMSE	SSIM	pSNR	NMSE	SSIM	pSNR	NMSE
fastMRI Knee	Random Rect.	0.9494	42.04	0.0032	0.9126	38.33	0.0063	0.8699	34.55	0.0134
	Equispaced Rect.	0.9520	42.68	0.0029	0.9163	38.78	0.0058	0.8758	35.04	0.0120
	Equispaced+ Rect.	0.9456	41.96	0.0034	0.9152	38.78	0.0059	0.8721	34.75	0.0126
	Gaussian 1D	0.9542	42.60	0.0028	0.9206	39.29	0.0053	0.8905	36.55	0.0088
	VDPD	<b>0.9653</b>	<b>44.54</b>	<b>0.0022</b>	<b>0.9376</b>	<b>41.39</b>	<b>0.0039</b>	<b>0.9181</b>	<b>39.52</b>	<b>0.0054</b>
	Gaussian 2D	0.9591	43.38	0.0025	0.9340	40.62	0.0045	0.9155	38.98	0.0062
	Radial	0.9555	43.26	0.0027	0.9348	41.07	0.0041	0.9169	39.27	0.0055
	Spiral	0.9567	43.41	0.0027	0.9365	41.25	0.0040	0.9196	39.60	0.0053
fastMRI Brain	Random Rect.	0.9708	43.05	0.0022	0.9466	38.23	0.0067	0.9102	33.23	0.0215
	Equispaced Rect.	0.9726	43.87	0.0019	0.9505	39.09	0.0055	0.9150	33.78	0.0183
	Equispaced+ Rect.	0.9689	42.97	0.0023	0.9489	38.79	0.0058	0.9126	33.44	0.0193
	Gaussian 1D	0.9729	43.57	0.0020	0.9534	39.62	0.0048	0.9264	35.35	0.0125
	VDPD	<b>0.9790</b>	<b>45.76</b>	<b>0.0012</b>	<b>0.9660</b>	<b>42.68</b>	<b>0.0024</b>	<b>0.9539</b>	<b>40.44</b>	<b>0.0039</b>
	Gaussian 2D	0.9758	44.23	0.0017	0.9637	41.79	0.0029	0.9518	39.94	0.0044
	Radial	0.9732	44.11	0.0018	0.9621	41.78	0.0029	0.9516	39.43	0.0049
	Spiral	0.9742	44.43	0.0016	0.9638	42.24	0.0027	0.9538	40.23	0.0041
Calgary Campinas	Random Rect.	0.9684	38.75	0.0031	0.9289	33.65	0.0104	0.8631	29.56	0.0264
	Equispaced Rect.	0.9756	41.02	0.0018	0.9364	34.57	0.0083	0.8709	30.05	0.0230
	Equispaced+ Rect.	0.9707	39.72	0.0025	0.9311	34.06	0.0093	0.8681	29.99	0.0235
	Gaussian 1D	0.9719	39.83	0.0024	0.9316	33.73	0.0099	0.8806	30.45	0.0220
	VDPD	<b>0.9809</b>	<b>42.80</b>	<b>0.0012</b>	<b>0.9643</b>	<b>38.70</b>	<b>0.0031</b>	<b>0.9465</b>	<b>35.97</b>	<b>0.0058</b>
	Gaussian 2D	0.9796	42.20	0.0014	0.9626	38.34	0.0034	0.9371	34.97	0.0074
	Radial	0.9767	41.47	0.0016	0.9594	37.75	0.0039	0.9324	34.22	0.0088
	Spiral	0.9774	41.82	0.0015	0.9621	38.46	0.0033	0.9385	35.12	0.0071

Table S4 : Model dependence experiments average quantitative results on the Calgary-Campinas dataset using RIMs instead of RecurrentVarNets. Bold numbers indicate the best across subsampling schemes.

Subsampling Scheme	Acceleration Factor (R)								
	2			4			8		
	SSIM	pSNR	NMSE	SSIM	pSNR	NMSE	SSIM	pSNR	NMSE
Random Rect.	0.9592	37.25	0.0044	0.9044	31.81	0.0159	0.8182	27.58	0.0424
Equispaced Rect.	0.9633	38.30	0.0034	0.9180	32.93	0.0119	0.8307	28.09	0.0361
Equispaced+ Rect.	0.9687	39.37	0.0027	0.9214	33.21	0.0112	0.8411	28.45	0.0331
Gaussian 1D	0.9681	38.78	0.0030	0.9180	32.47	0.0132	0.8277	27.86	0.0382
VDPD	<b>0.9768</b>	<b>41.87</b>	<b>0.0015</b>	<b>0.9620</b>	<b>38.36</b>	<b>0.0033</b>	<b>0.9431</b>	<b>35.64</b>	<b>0.0063</b>
Gaussian 2D	0.9755	41.29	0.0017	0.9600	37.94	0.0037	0.9354	34.85	0.0076
Radial	0.9719	40.60	0.0020	0.9568	37.37	0.0043	0.9303	33.93	0.0094
Spiral	0.9727	40.88	0.0019	0.9586	37.83	0.0038	0.9343	34.51	0.0082